Received: 1 January 2022 | Revised: 9 March 2022 | Accepted: 4 April 2022 | Published on: 18 April 2022

DOI: 10.1002/joc.7647

International Journal of Climatology RMetS

RESEARCH ARTICLE

The characteristics of mesoscale convective systems generated over the Yunnan–Guizhou Plateau during the warm seasons

Yuanjing Guo[1,2] | Yu Du[3,4] | Riyu Lu[1,2] | Xinxian Feng[1,2] | Jun Li[5] | Yuanchun Zhang[6] | Zi Mai[7]

[1]State Key Laboratory of Numerical Modeling for Atmospheric Sciences and Geophysical Fluid Dynamics, Institute of Atmospheric Physics, Chinese Academy of Sciences, Beijing, China

[2]College of Earth and Planetary Sciences, University of the Chinese Academy of Sciences, Beijing, China

[3]School of Atmospheric Sciences, Guangdong Province Key Laboratory for Climate Change and Natural Disaster Studies, Key Laboratory of Tropical Atmosphere-Ocean System, Sun Yat-sen University, Zhuhai, China

[4]Southern Marine Science and Engineering Guangdong Laboratory (Zhuhai), Zhuhai, China

[5]31010 PLA Troops, Beijing, China

[6]Key Laboratory of Cloud-Precipitation Physics and Severe Storms (LACS), Institute of Atmospheric Physics, Chinese Academy of Sciences, Beijing, China

[7]National Meteorological Center, China Meteorological Administration, Beijing, China

Correspondence
Yu Du, School of Atmospheric Sciences, Guangdong Province Key Laboratory for Climate Change and Natural Disaster Studies, Key Laboratory of Tropical Atmosphere-Ocean System, Sun Yat-sen University, Zhuhai, Guangdong 519082, China.
Email: duyu7@mail.sysu.edu.cn

Funding information
Guangdong Major Project of Basic and Applied Basic Research, Grant/Award Number: 2020B0301030004; National Natural Science Foundation of China, Grant/Award Numbers: 42122033, 41875055, 42075006; Guangzhou Science and Technology Plan Projects, Grant/Award Number: 202002030346

Abstract

The characteristics of mesoscale convective systems (MCSs) over the Yunnan–Guizhou Plateau (YGP) during the warm seasons (April–August) are investigated using an automatic tracking algorithm based on long-term (2000–2018) hourly geostationary satellites data of temperature of black body. A total of 1,845 MCSs generated over the YGP are identified and further classified into the eastward moving type (EMT; ~13.1%) and noneastward moving/dissipating type (NDT; ~86.9%). The two types of MCSs exhibit varying characteristics. The EMTs are mainly active in the eastern flank of the YGP with a longer mean lifespan (~16.5 hr), while the NDTs occur anywhere over the YGP with a preference for the central YGP with a shorter mean lifespan (~7.6 hr). The MCSs are observed most frequently during June–July, while the ratio of EMTs reaches the highest in April due to the strongest steering flows. The abundant moisture supply plays a vital role in the generation and development of MCSs in June, whereas the dynamic forcing and high CAPE are favourable to MCSs in July. In terms of the diurnal cycle, the NDTs are generally initiated in the afternoon, reach mature in the late afternoon, and dissipate at night. By contrast, the mature stage of EMTs shows double diurnal peaks in the late afternoon and early morning. The MCSs are usually generated in an instable environment accompanied by strong vertical wind shear and intense low-level water vapour flux over the YGP, and the MCSs tend to vacate the YGP with strong mid-level westerlies and instable environment in the downstream regions. Compared to MCSs in Tibetan Plateau, the ratio of the EMTs is higher with longer lifespans though fewer MCSs are generated over the YGP.

KEYWORDS
characteristics, cloud cluster tracking, mesoscale convective system, precipitation, Yunnan–Guizhou Plateau

1 | INTRODUCTION

Mesoscale convective systems (MCSs) are the organized cumulonimbus clouds that aggregate and interact to induce a single entity with a horizontal dimension of hundreds of kilometres and a temporal dimension of several hours or even longer (Laing and Michael, 1997; Schumacher and Rasmussen, 2020). MCSs make an obvious contribution to total precipitation in the tropical and mid-latitude areas and are crucially important to the global hydrologic cycle (Houze *et al*., 1990; Feng *et al*., 2019; Roca and Fiolleau, 2020; Feng *et al*., 2021; Liu *et al*., 2021; Zhao, 2022). Besides, MCSs, as typical severe convection weather systems, can cause destructive weather events such as severe winds, lightning, hail, flooding, and tornadoes (Houze *et al*., 1990; Doswell *et al*., 1996; Feng *et al*., 2016; Schumacher and Rasmussen, 2020).

After Maddox (1980) first identified mesoscale convective complexes (MCCs, a subset of MCSs) through early infrared imagery, MCSs have been widely studied all over the world. For instance, the United States Great Plains, to the east of the Rocky Mountains, is one of the hot spots of the most intense MCSs in the globe. The MCSs over the Great Plains have strong seasonal variation with a maximum in May–June (Feng *et al*., 2019). The MCSs produce over 50% of rainfall during the warm seasons in most regions of the contiguous United States, particularly to the east of the Rocky Mountains (Feng *et al*., 2016; Haberlie and Ashley, 2019). Africa is another high-frequency centre of intense MCSs. Laing and Fritsch (1993) pointed out that the MCSs over Africa display similar features as those over America, although they occur within considerably different large-scale settings. Unlike the eastward propagating MCSs in the United States, the MCSs over northern Africa are usually found to move westward (Payne and McGarry, 1977; Mathon *et al*., 2002). When the deep convection develops well, the MCSs move westward at a greater propagation speed (Mathon and Laurent, 2001).

The generation and development of MCSs are influenced by large-scale circulations as well as local effects. The development environment of MCSs often features prominent dynamic and thermodynamic characteristics (Zeng *et al*., 2016; Zheng and Sun, 2016). The upper-level divergence contributes to MCSs' formation and development (Li *et al*., 2015; Mai *et al*., 2021). MCSs are usually initiated ahead of large-scale troughs in the westerlies because of the large-scale lifting (Maddox, 1983; Yang *et al*., 2020). Low-level thermal forcing, convergence, and conditional instability favour the evolution of MCSs (Augustine and Howard, 1991). The low-level jet (LLJ) is also essential for the initiation and development of MCSs by affecting the instability of atmospheric stratification (Trier and Parsons, 1993) and convergence (Du and Chen, 2019).

MCSs will impact the downstream if they vacate their generation areas. The possible reasons have also been explored in the previous studies. In the upper troposphere, the larger zonal temperature gradient may cause stronger warm temperature advection, contributing to MCSs moving downstream through causing pressure lowering (Markowski and Richardson, 2010). The mean flow at middle–high levels, acting as steering flows, could also influence MCS's movement (Jiang *et al*., 1996). Furthermore, strong vertical wind shear over the initiation locations and the downstream regions of MCSs could promote the development and movement of convection (Schumacher and Johnson, 2005; DeLonge *et al*., 2010).

Compared to the MCSs over the United States and Africa, the studies regarding the MCSs over East Asia are relatively less. Li *et al*. (2012) investigated the MCSs over East Asia in the warm season and suggested that high-frequency centres of the MCSs distribute in the low latitudes, and moderate-frequency centres distribute in the middle latitudes. Since the terrain in China is complex, significant regional differences of MCSs exist in their spatial and temporal variations (Ma *et al*., 1997; Zheng *et al*., 2008). The MCSs formed over the Tibetan Plateau (TP) and Middle East China are most active in July, while those over South China are active in June (Zheng *et al*., 2013; Li *et al*., 2015; Mai *et al*., 2021; Zhang *et al*., 2021). The life cycles of MCSs in different regions are also varied. For instance, the MCSs over the TP manifest single-peak pattern all day long, while the MCSs over Middle East China show multi-peaks pattern (Zheng *et al*., 2008; Qi and Zheng, 2009). The initiation and dissipation peak of the MCSs over the TP occurs in the afternoon and at night, respectively (Fu *et al*., 2013; Zhang *et al*., 2021). The MCSs over the Sichuan Basin have an obvious nocturnal feature, which are more active after midnight and become weaker in the afternoon (Zheng *et al*., 2008). In Middle East China, the MCSs mainly form in the late afternoon around 1800 LST (UTC + 8) and the early morning around 0600 LST. The developing and dissipative stages are significantly longer as the total durations of MCSs increase. As the MCSs dissipate after maturity, they also have double peaks in the morning around 0900 LST and at midnight around 0300 LST (Dai, 2001; Ai *et al*., 2016). Moreover, the MCSs over the ocean frequently initiate earlier than over the land and have longer lifespans and higher precipitation production (Chen *et al*., 2020; Feng *et al*., 2021). However, the life cycles and lifespans of MCSs over the YGP are still not well known.

Previous studies on the MCSs over China mainly focus on the TP and its downstream (the Yangtze or Huai River Valley). The studies of MCSs activities over the second-step terrain remain scarcer (Yang *et al.*, 2020). Particularly, the Yunnan–Guizhou Plateau (YGP) is one of the four famous plateaus in China, which is located in the low latitudes and can be influenced by both the tropical and subtropical synoptic systems. The MCSs over the YGP often cause sudden local torrential rains and severe natural disasters (e.g., flood, landslide, and debris flow) and thus result in huge economic losses and serious numbers of casualties. Moreover, the east-moving MCSs generated over the YGP can further influence south China, just as the east moving MCSs generated over the TP have impacts on the middle and lower reaches of the Yangtze River. Therefore, the MCSs generated over the YGP are necessary to investigate and compare with the MCSs of TP. Understanding on characteristics of MCSs generated over the YGP would help improve convective weather forecasts. However, the previous studies are scarce and cover relatively short periods or use manual method to track MCSs (e.g., Duan *et al.*, 2004; Yang *et al.*, 2015).

Therefore, we examine statistical characteristics of the MCSs of the YGP in the warm season (April–August) using new satellite data and objective tracking method on a long analysis period time and explore the main factors governing the generation and evolution of the MCSs. Due to the short duration and the small scale of the MCSs, geostationary satellites with high spatiotemporal resolution are effective tools to monitor them. In addition, the leading scientific questions in the present study include (a) What are the environmental conditions conducive to the generation of the MCSs? What influences the monthly variations of the MCSs? (b) What percentage of the MCSs can propagate out of the YGP and further affect the downstream regions? What are the differences between the propagating MCSs and the non-propagating MCSs? Which factors influence the movement of the MCSs? (c) What are the differences between the MCSs over the YGP and TP?

The organization of this article is as follows. The data and methodology used in this study are presented in section 2. In section 3, we explore the statistical features of MCSs generated over the YGP, including their tracks, lifespans, spatial distribution, temporal variations, and so on. Section 4 describes the environmental conditions related to the MCSs. The environmental conditions are compared between MCS and non-MCS events and between propagating MCS and non-propagating MCS events. In section 5, we compare the characteristics of MCSs generated over the YGP and TP. Finally, section 6 summarizes the results.

2 | DATA AND METHODOLOGY

2.1 | Data

The MCSs in this study are identified using hourly $0.05^\circ \times 0.05^\circ$ temperature of black body (TBB) observed by five geostationary satellites (GMS-5, GOES-9, MTSAT-1R, MTSAT-2, Himawari-8) in the infrared range (IR1) provided by the Japanese Meteorological Agency. The channel IR1 lies on the infrared window region, which is essential for measuring sea and land surface and cloud-top temperatures (Schmetz *et al.*, 2002; Tahara *et al.*, 2004; Li, 2010). Thus, IR1 channel images have been widely used to identify the MCSs according to the previous research (e.g., Maddox, 1980; Mathon and Laurent, 2001; Ai *et al.*, 2016; Núñez Ocasio *et al.*, 2020; Mai *et al.*, 2021). The periods and specifications of each satellite used in this study are shown in Table 1. Although the TBB data are derived from different satellites, the errors caused by using various sensors and/or data processing programs are acceptable (the differences of TBB among these satellites are less than 1 K) according to Tahara *et al.* (2004) and Murata *et al.* (2015). Since the MCSs over YGP occur more frequently in the warm seasons (Duan *et al.*, 2004; Yang *et al.*, 2015), we focus on the period of April–August in this study. The period of the present study covers the warm seasons from 2000 to 2018 excluding 2005 because the data missing rate in 2005 is high.

Considering the high temporal and spatial resolution of satellite TBB data, we use hourly $0.0727^\circ \times 0.0727^\circ$ National Oceanic and Atmospheric Administration CPC Morphing Technique (CMORPH) high-resolution precipitation data (Joyce *et al.*, 2004) instead of other relatively coarse resolution precipitation data (e.g., TRMM; 3 hr and 0.258°). Since the precipitation data is utilized to show the spatial distribution of MCS-related precipitation

TABLE 1 Periods and specifications of each satellite used in this study

Satellite	Period	Infrared wavelength (μm)
GMS5	April 1, 2000, 0000 UTC–May 21, 2003, 2300 UTC	11.0
GOE9	May 22, 2003, 0000 UTC–August 31, 2004, 2300 UTC	10.7
MTSAT-1R	April 1, 2006, 0000 UTC–August 31, 2010, 2300 UTC	10.8
MTSAT-2	April 1, 2011, 0000 UTC–July 1, 2015, 2300 UTC	10.8
Himawari-8	July 7, 2015, 0000UTC–August 31, 2018, 2300 UTC	10.4

rather than to track MCSs, we use its original data without interpolation. Although the spatial resolution of the TBB data and precipitation data are not the same, the error is small enough to be ignored. Besides that, the hourly $0.25° \times 0.25°$ ERA5 reanalysis data (Hersbach *et al.*, 2020) are applied to composite the background circulation. Since the use of the reanalysis data is intended to examine large-scale circulation associated with MCSs, rather than resolve convective-scale features, we keep its original resolution without interpolation.

2.2 | Methodology

The criteria we used for identifying the MCSs generated over the YGP are as below:

1. The generation location of the MCS is within the region 23°–28°N, 100°–108°E (the white dashed box in Figure 1).
2. The area of the contiguous cloud structure with TBB $\leq -52°C$ exceeds 5,000 km^2. Zheng *et al.* (2008) pointed out that applying the criterion of TBB $\leq -52°C$ could show the spatial and temporal distribution characteristics of MCSs over China and its vicinity. Yang *et al.* (2015) used −52°C as the standard of MCSs over YGP. The area standard we used in this study refers to Mathon and Laurent (2001). According to their studies, the area criterion cut-off of 5,000 km^2 does not significantly affect the total number and lifespan of tracked MCSs compared with manual tracking. The area standard has been widely applied to track the MCSs throughout their lifetimes (e.g., Li *et al.*, 2012; Ogungbenro *et al.*, 2016; Mai *et al.*, 2021; Zhang *et al.*, 2021).
3. The duration of satisfying the above criteria exceeds 3 hr. According to the Navier–Stokes equations, the time scale of an MCS is f^{-1} (f refers to the Coriolis parameter) which is about 3 hr in the middle latitude (Parker and Johnson, 2000).

The generation time is defined as when an MCS satisfies the criterion for the first time, and the dissipation time is defined as when the MCS no longer meets the criterion or merges with a larger one. The maturation time of an MCS is defined as when the MCS attains maximum area.

We use the automatic tracking algorithm developed by Li (2010) to recognize and track the MCSs. The specific steps are as follows:

1. Remove noise interferences from the TBB data files by a 9-point smoothing method.
2. Read the TBB data files in sequence and identify MCS cells according to the above criteria.
3. Match MCSs identified at time t and time $t + 1$ to verify if they are the same one by using three standards, including distance standard, R-descriptor standard (Lu *et al.*, 1987), and Hu-moment standard (Hu, 1962).
4. Repeat the above steps 2–3 until there is no TBB data file left.

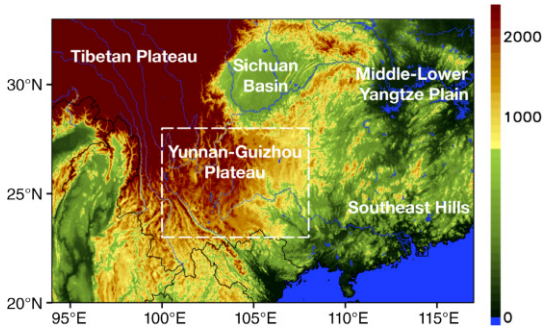

FIGURE 1 Terrain height around the YGP (shading; units: m). The dashed box (23°–28°N, 100°–108°E) denotes the YGP [Colour figure can be viewed at wileyonlinelibrary.com]

Although this tracking algorithm is effective and accurate, it cannot track precisely when clouds are split and merged. Hence, we further check and correct (if necessary) every tracked MCSs manually. Based on the correction methods documented in Mathon and Laurent (2001) and Feng *et al.* (2012), the manual correction method in this study includes three key procedures: (a) when two or more MCSs merge together, the largest MCS is assumed to continue, while the smaller ones are terminated; (b) when an MCS splits into several smaller systems, the largest MCS continues carrying the characteristics of the original system and the smaller parts that satisfy the MCS's criteria are assumed as newly-born MCSs; (c) the corrected MCSs must satisfy the criteria used in the automatic tracking algorithm. Therefore, the tracking method used in the present research is a combination of subjective and objective tracking.

Following previous studies on MCSs of the TP (Fu *et al.*, 2011; Mai *et al.*, 2021), the YGP MCSs could also be divided into two types: (a) eastward moving type [EMT] (those moving eastward and vacating the YGP) and (b) non-eastward moving/dissipating type [NDT] (those not moving eastward or doing so but dissipating over the YGP). What's more, 108°E is defined as the eastern boundary of the YGP, so vacating the YGP just refers to moving farther east to 108°E in this study.

We further classify the EMTs into two categories based on their lifespans: (a) longer-lived-EMTs [L-EMTs] (those that persist for at least 6 hr in their lifespans and

last for at least 3 hr after vacating the YGP) and (b) shorter-lived-EMTs [S-EMTs] (those that persist for less than 6 hr in their lifespans or vanish within 3 hr after vacating the YGP), following Mai *et al.* (2021). Besides, based on their moving directions, EMTs are classified as northeastward moving EMTs, southeastward moving EMTs, and eastward moving EMTs. The displacement vector is defined as the starting location of an EMT (the average location of an EMT at its first 2 hr) to the ending location (the average location of an EMT at its last 2 hr). If the angle between the displacement vector and the zonal direction is greater (less) than 30° (−30°), we define the EMT as northeastward moving (southeastward moving) EMT; if the angle is between ±30°, we define it as eastward moving EMT.

We estimate the MCS-related precipitation using the parameters from the tracking algorithm. The method we used, according to Ai *et al.* (2016), is as below. We identify an MCS's outline as a closed curve through the tracking algorithm. The closed curve can be seen as an approximate ellipse with its long and short axes, which can be used to draw a rectangle tangent to this ellipse. Then we can identify a circle by using the diagonal of this rectangle as the diameter. The precipitation in the circle during the tracking range is defined as the precipitation related to an MCS. We calculate the hourly precipitation of all MCSs at all grids and then sum them all during the study period. Finally, we divide the summation of MCS-related precipitation by total local precipitation in the same tracking region during all the warm seasons. This ratio is defined as the contribution of MCS-related precipitation to the total local precipitation.

In addition, in section 4, we investigate the environmental conditions related to MCSs through composite analyses. We also perform anomaly analyses, which are calculated as the deviations between the original data and multi-year (2000–2018) averages for particular times and days based on the hourly dataset.

3 | STATISTICAL CHARACTERISTICS OF MCSS

3.1 | Tracks, lifespan, and spatial distribution

A total of 1,845 MCSs generated over the YGP are tracked in the warm seasons from 2000 to 2018, excluding 2005. Figure 2 presents the tracks of total MCSs, EMTs, and NDTs. The EMTs account for ∼13.1% of total MCSs, and the remaining (∼86.9%) are NDTs (Figure 3a). The mean lifespan of the EMTs (16.5 hr) is more than twice as long as that of the NDTs (∼7.6 hr), suggesting the EMTs persist for a much longer period. The longest lifespan of EMTs is ∼67 hr, while that of NDTs is ∼54 hr. For either EMTs or NDTs, shorter-lived MCSs predominate (Figure 3b). However, the long-lived EMTs make up a higher proportion of their total amounts than that of NDTs. Only ∼39.0% of NDTs last for more than 6 hr, while around 79.8% of EMTs can do so. Particularly, the ratio of EMTs with lifespans more than 36 hr reaches 4.1%, which is much higher than NDTs (∼0.7%). The contribution of NDT numbers to their total numbers decreases along with the increases in lifespans.

Figure 4a–c shows the locations of EMTs and NDTs during the stages of generation, maturation, and dissipation. The EMTs often generate in the eastern section of the YGP, while the NDTs can form over the YGP evenly (Figure 4a). The maturation locations of the EMTs show an evident eastward shift compared to their generation locations, and the dissipation locations of the EMTs occur farther east than 108°E (Figure 4b,c). In addition, the NDTs become more scattered from maturation to dissipation period (Figure 4b,c).

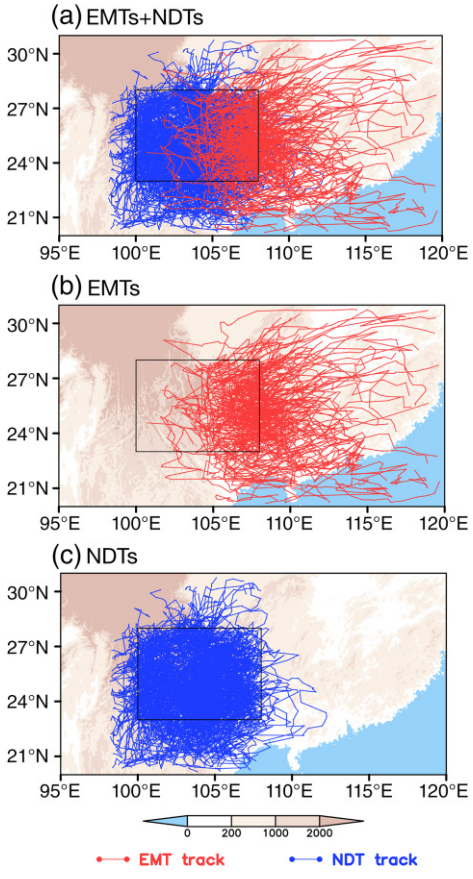

FIGURE 2 The tracks of (a) total MCSs, (b) EMTs, and (c) NDTs. The box denotes the study area [Colour figure can be viewed at wileyonlinelibrary.com]

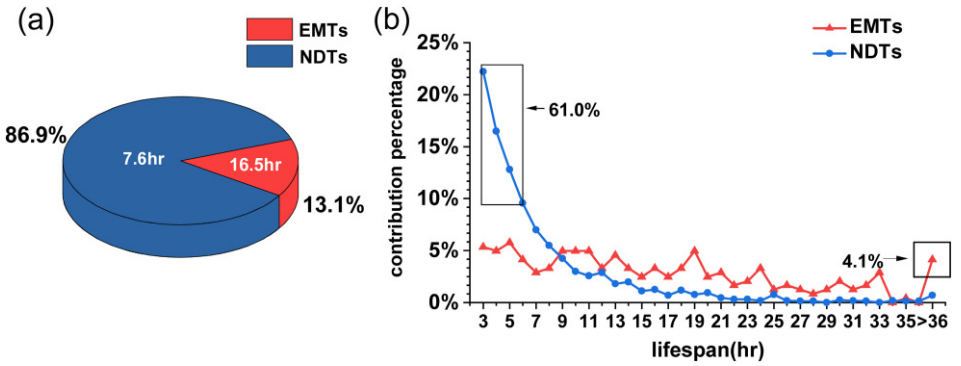

FIGURE 3 (a) The EMT and NDT numbers proportion of the total MCS numbers and their corresponding average lifespans and (b) the contribution (%) of EMT and NDT numbers along with the varying lifespans to the total EMT numbers and NDT numbers, respectively [Colour figure can be viewed at wileyonlinelibrary.com]

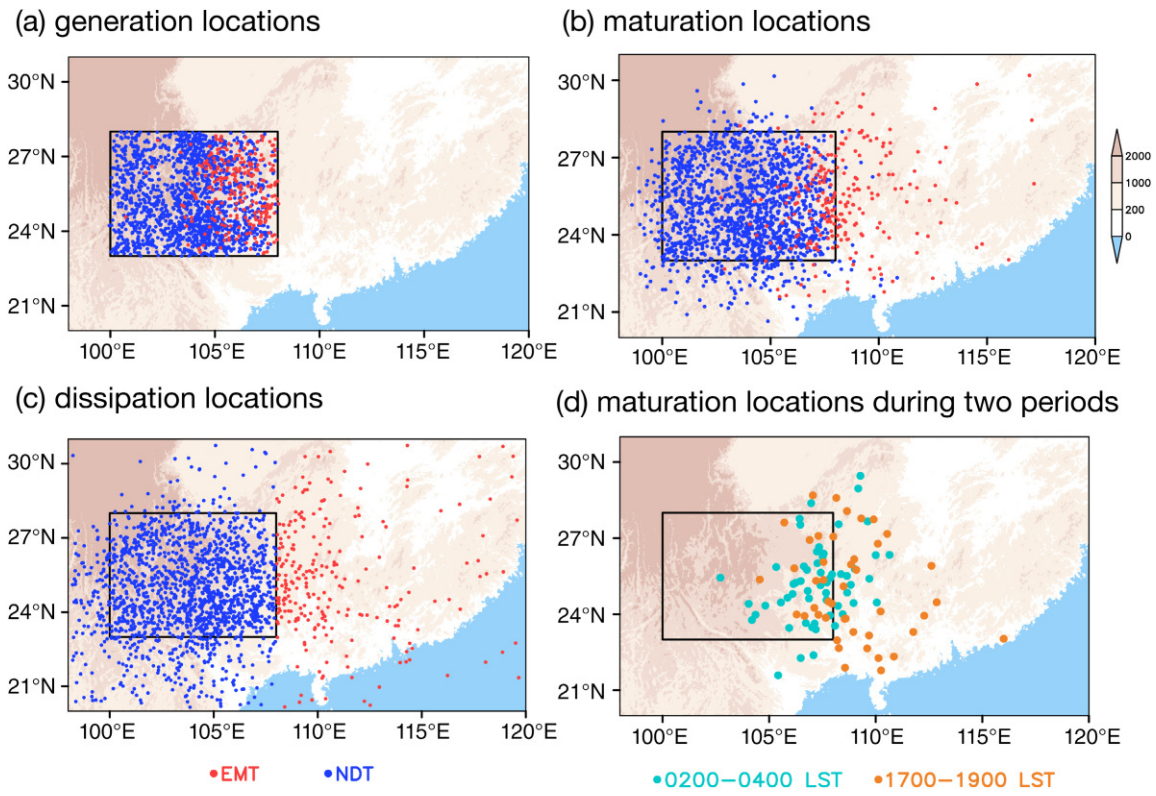

FIGURE 4 Spatial distribution of locations where EMTs and NDTs (a) generate, (b) become mature, and (c) dissipate. (d) The spatial distribution of locations where the EMTs become mature during 0200–0400 LST and 1700–1900 LST [Colour figure can be viewed at wileyonlinelibrary.com]

Figure 5 shows the spatial distribution of MCS activity frequency. The EMTs are mainly observed in the regions east of 104°E, including the eastern flank of the YGP, eastern Guangxi, and western Guangdong (Figure 5b), while the NDTs occur in the central YGP more frequently (Figure 5c). The maximum centre of activity frequency of the total MCSs (Figure 5a) appears over the east-central YGP, consistent with Duan *et al.* (2004). The centre is mainly contributed by the NDTs due to their higher frequency.

The MCSs over the YGP can produce rainfall over the YGP and its vicinity during the warm seasons, and the contribution of EMT- and NDT-related precipitation to the total local precipitation are varied, as shown in Figure 6. The MCS-related precipitation can affect the YGP and its downstream regions and has a maximum contribution center in the eastern section of the YGP (Figure 6a). The maximum contribution areas of EMT- and NDT-related precipitation are generally consistent with their active regions shown in Figure 5. The EMT-related precipitation makes an obvious contribution to the total local precipitation in the eastern flank of the YGP and the downstream regions (Figure 6b). Compared to the EMTs, the NDTs mainly produce precipitation on

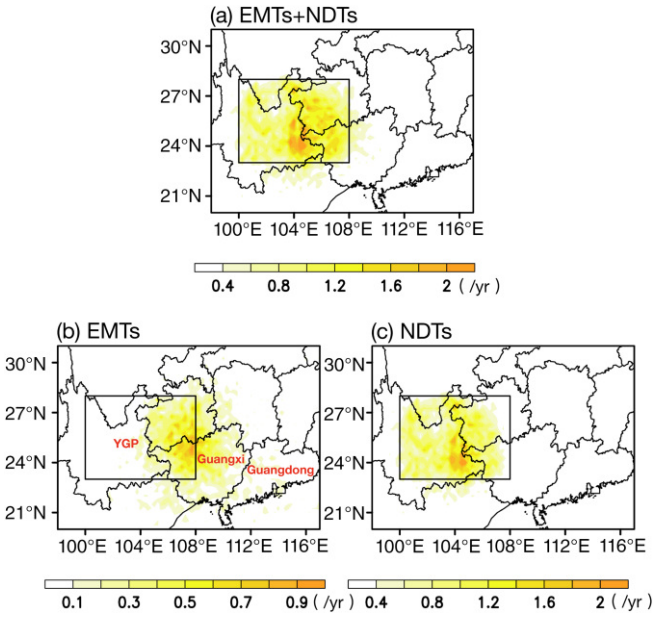

FIGURE 5 The spatial distribution of occurrence (shading; units: year^{-1}) of (a) total MCSs, (b) EMTs and (c) NDTs [Colour figure can be viewed at wileyonlinelibrary.com]

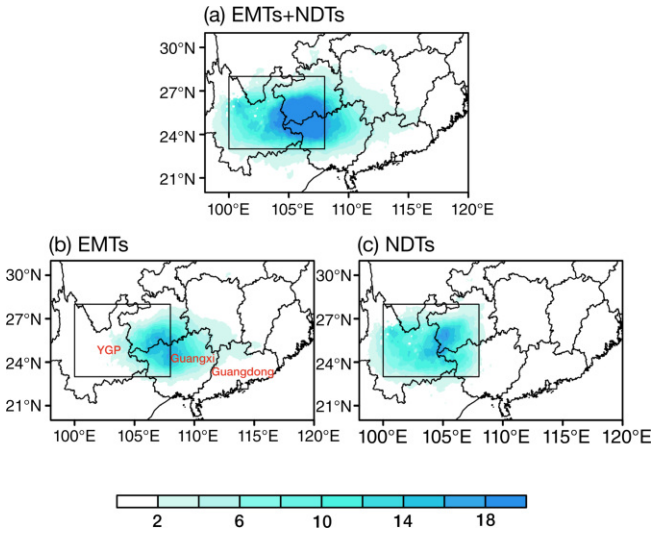

FIGURE 6 The spatial distribution of percentage contribution (shading; units: %) of (a) MCS-related, (b) EMT-related, and (c) NDT-related precipitation to total local accumulated precipitation during the warm seasons [Colour figure can be viewed at wileyonlinelibrary.com]

the YGP (Figure 6c). It is noted that the maximum precipitation contributions of the EMTs and NDTs to total accumulated precipitation during the warm seasons are similar (~18%), but the number of the EMTs is far less than that of the NDTs. Therefore, the result suggests that the EMT-related rainfall is more intense than NDT-related rainfall.

Since the EMTs are likely to influence the downstream significantly, they are further classified and examined. Figure 7 compares the tracks of different kinds of EMTs. The L-EMTs proportion (~71.0%) is much higher than that of S-EMTs (~29.0%). The ratio of the eastward moving EMTs is highest (~77.6%), followed by the southeastward moving EMTs (~13.3%) and northeastward moving EMTs (~9.1%). The number of L-EMTs is larger than S-EMTs in all directions, while the eastward moving EMTs dominate in both L-EMTs and S-EMTs. What's more, for L-EMTs, the ratio of southeastward moving events (~15.2%) is higher than that of northeastward moving events (~6.4%). On the contrary, for the S-EMTs, the contribution of southeastward moving events (~8.6%) is less than northeastward moving events (~15.7%). Therefore, southeastward moving EMTs tend to last for a longer time compared to northeastward moving EMTs. In addition, the mean lifespan of L-EMTs is ~20.3 hr, and that of S-EMTs is ~7.2 hr. The lifespans of EMTs for different directions are also varied, especially for L-EMTs: the mean lifespan is longer for southeastward moving L-EMTs (~25.0 hr) compared to the northeastward moving (~11.5 hr) and eastward moving (~20.1 hr) L-EMTs.

3.2 | Temporal variations

3.2.1 | Interannual variations

During the warm seasons, the average amount of MCSs formed over the YGP is 102.5 per year. However, the number of MCSs exhibits significant interannual variations: the maximum number of MCSs is 133 in 2000, and the minimum one is 74 in 2011 (Figure 8a). In addition, the average contribution of the EMTs to total MCSs is ~13.4%, with the highest one (~22.6%) in 2007 and the lowest one (~5.7%) in 2013 (Figure 8b). No obvious interdecadal variability is found during the studied period.

3.2.2 | Monthly variations

Figure 9 shows the number of MCSs and the proportion of the EMTs in each month of the warm season. The MCSs occur most frequently in June (~32.2) and July (~30.7) but occur least in April (~4.6) (Figure 9a). The number of MCSs in June–July makes up more than 60.0% of total MCS numbers. By contrast, the proportion of EMTs is the greatest in April (~50.0%) and the lowest in August (~3.1%) (Figure 9b). The reasons for the significant monthly variations will be explained in section 4.

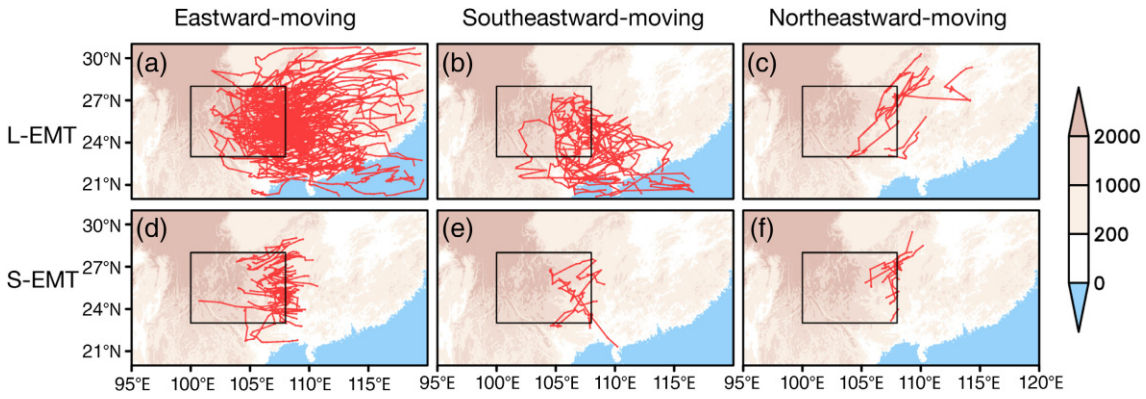

FIGURE 7 Tracks of different kinds of EMTs: (a, d) eastward moving, (b, e) southeastward moving, and (c, f) northeastward moving EMTs with (a–c) longer lifespans and (d–f) shorter lifespans [Colour figure can be viewed at wileyonlinelibrary.com]

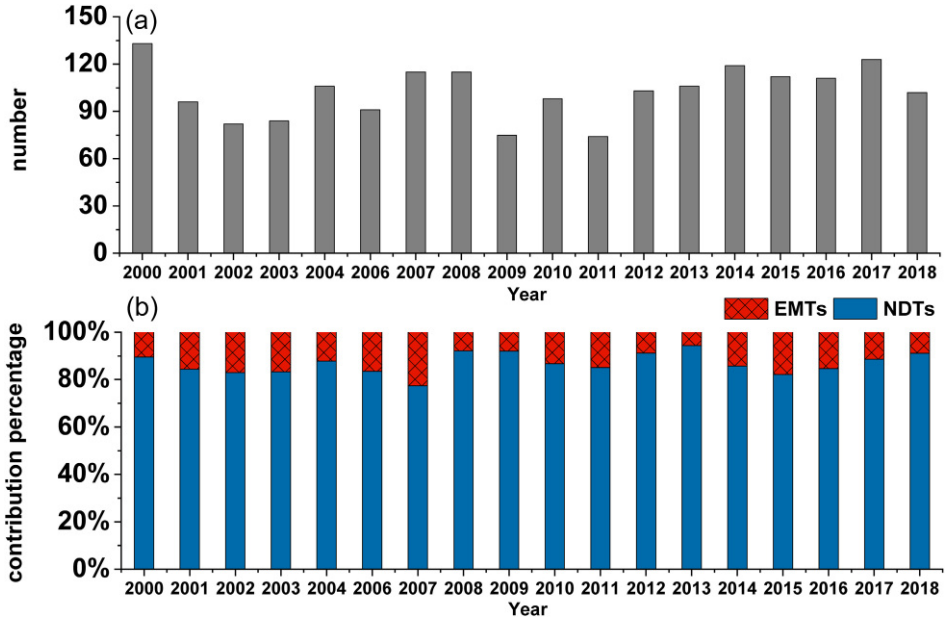

FIGURE 8 (a) The interannual variations of MCS occurrence numbers and (b) percentage contribution of EMTs and NDTs to the total number of MCSs [Colour figure can be viewed at wileyonlinelibrary.com]

3.2.3 | Diurnal variations

In general, the generation number of MCSs reaches its peak in the afternoon (Figure 10a), while the MCSs often vanish at night (Figure 10e). The maturation of MCSs manifests double peaks in the late afternoon and the early morning (Figure 10c).

We further investigate the diurnal variations of the two types of MCSs. The generation of both EMTs and NDTs reach peaks at around 1500–1600 LST (UTC + 7) (Figure 10b), probably due to the strongest surface temperature and thermal convection in the late afternoon. The NDTs subsequently reach the maturation peak after 3 hr of the generation peak. By contrast, the maturation of the EMTs shows double peaks, which are in the late afternoon (~1700–1900 LST) and the early morning (~0200–0400 LST) (Figure 10d). The results are consistent with Zheng *et al.* (2007, 2008), which suggested that the multi-peak MCSs have a longer life cycle (get weaker after sunset and develop again in the early morning). The late afternoon peak of the EMTs at the maturation stage can be explained by the strongest

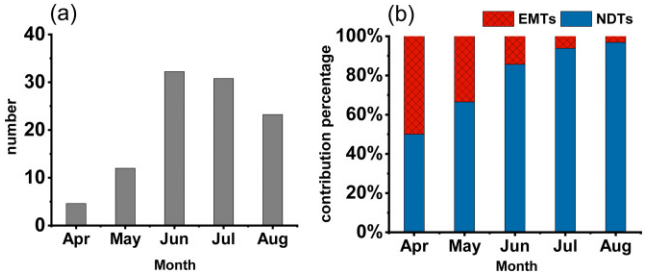

FIGURE 9 As in Figure 8, but for the monthly variations [Colour figure can be viewed at wileyonlinelibrary.com]

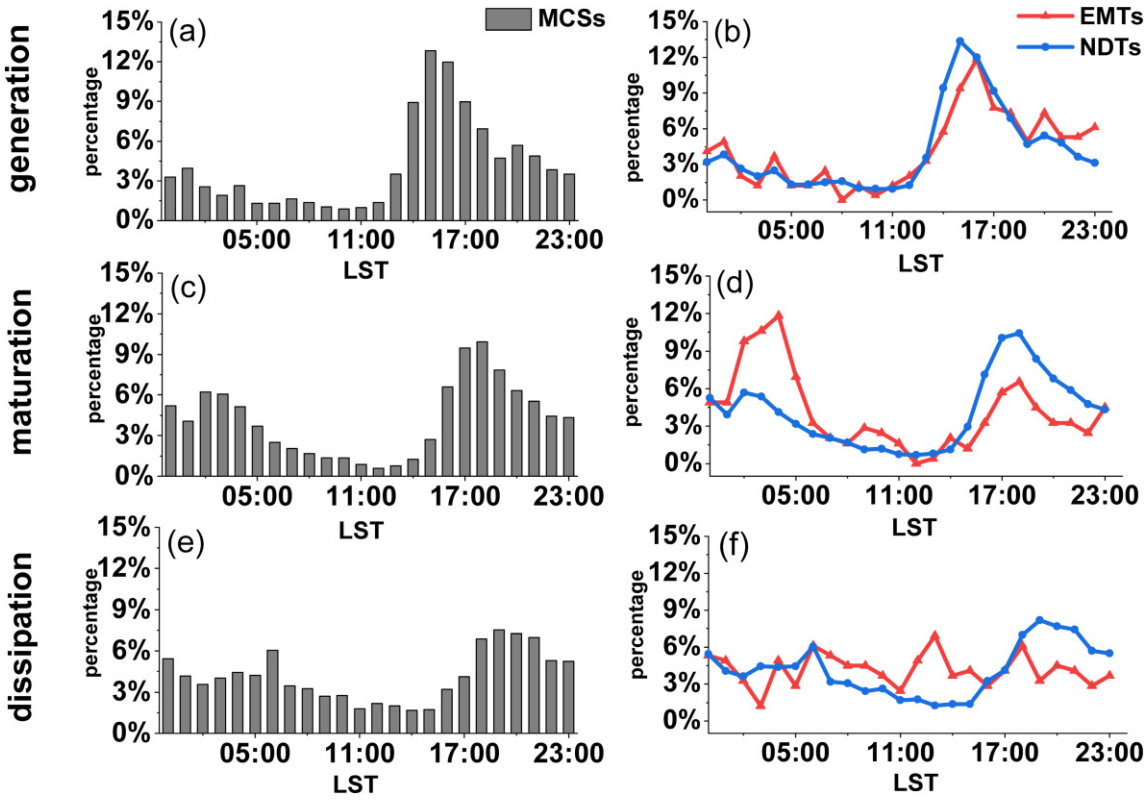

FIGURE 10 The left panels show the diurnal variations in the percentage contribution of the MCSs to the total MCS numbers during the (a) generation, (c) maturation, and (e) dissipation stage. (b–f) The right panels are the same as the left ones, but for EMTs and NDTs [Colour figure can be viewed at wileyonlinelibrary.com]

surface longwave radiation and turbulence transportation (Li *et al.*, 2012) which is the same as NDTs' maturation peak.

Furthermore, the early morning peak of the EMTs might be caused by the redevelopment of MCSs. One of the possible reasons for the nocturnal redevelopment is the longwave cooling radiation from the cloud top in the early morning, which results in a significant temperature difference between the cloud top and bottom, and thus promotes the convection (Duan *et al.*, 2004; Li *et al.*, 2012). In addition, the mountain-valley wind circulation caused by the thermal difference between the YGP and the downstream plains can induce the convergence at the foothill of the plateau in the early morning and thus favours the development and eastward movement of MCSs (Zheng *et al.*, 2008). Meanwhile, the nocturnal low-level jet around the mountain plays a vital part in nocturnal EMTs' evolution (Augustine and Caracena, 1994; Salio *et al.*, 2007; Du *et al.*, 2014). On the one hand, the instability of atmospheric stratification is intensified by the transportation of low-level warm and moist air. On the other hand, the convergence and upward motion ahead of the maximum wind velocity centre of the jet provide the dynamic conditions and abundant moisture necessary for EMTs' development.

Therefore, the maturation EMTs during the period of ~0200–0400 LST are mainly confined in the eastern flank of the YGP, while the maturation EMTs during the period of ~1700–1900 LST tend to be more scattered, as shown in Figure 4d. The NDTs often dissipate over the YGP at around 1900–2100 LST due to the cooling effect of plateau after sunset. On the contrary, the dissipation of the EMTs exhibits little diurnal variations (Figure 10f) because EMTs can vanish at various timing and locations due to their long lifespans when the environment becomes unfavourable.

4 | ENVIRONMENTAL CONDITIONS RELATED TO THE MCSS

4.1 | Comparisons in the environmental conditions between MCS and non-MCS events

This section examines the dynamic and thermodynamic environmental conditions conducive to the generation and development of MCSs by comparing the MCS and non-MCS events based on the hourly dataset. In the mid-

level (500 hPa), a significant trough exists over South Asia (60°–90°E, 10°–30°N) during the MCS events, whereas the trough is weaker during the non-MCS events as shown in Figure 11a,b. The trough favours mid-level quasi-geostrophic forcing associated with cyclonic vorticity advection and warm temperature advection ahead of the trough (Holton, 2004). That could induce ascending motion and convection over the YGP, which is conducive to the organization and evolution of the MCSs. Figure 11c further presents the difference in divergence between the MCSs and non-MCS events at a lower level (700 hPa). The low-level convergence over the YGP during the MCS events is stronger than that during the non-MCS event. This configuration provides conducive mid-level quasi-geostrophic forcing and low-level convergence, both of which are favourable to ascending.

The southwesterlies at 700 hPa over the southwestern region of China during MCS events are stronger than that during non-MCS events (Figure 12a,b), which could transport more water vapour. The equation of water vapour flux is as follow:

$$|F_H| = \frac{1}{g}|V|q, \tag{1}$$

where F_H stands for horizontal water vapour flux, g is acceleration of gravity, V is horizontal wind velocity, and q is specific humidity. The maximum centres of low-level water vapour flux during the MCS events over the YGP ($\sim$8.0 g·s·kg^{-1}) and downstream ($\sim$7.5 g·s·kg^{-1}) are relatively larger than those during the non-MCS events ($\sim$6.5 g·s·kg^{-1}; $\sim$6.5 g·s·kg^{-1}). What's more, as documented in the previous studies, the wind shear in low levels is also an essential factor in the formation and development of the MCSs (Rotunno *et al.*, 1988; Moncrieff, 1992; Chen *et al.*, 2015). As shown in Figure 11d, the 0–3 km vertical wind shear during MCS events is larger than during non-MCSs either over the YGP or downstream. It is noted that the MCS events occur more frequently in June–July, while the non-MCS events mainly occur in April–May. Considering that the composite differences of the 0–3 km vertical wind shear between MCS and non-MCS events mainly include the climatological differences between June–July and April–May, we perform anomaly analyses of 0–3 km vertical wind shear. In this way, the seasonal difference could be removed and the difference between the MCSs and non-MCS events could be shown clearly.

Figure 12c shows the height-longitudinal cross section of potential pseudo-equivalent temperature (θ_{se}) averaged over 23°–28°N for the MCS events. The θ_{se} during the MCS events decreases significantly as the altitude increases below 600 hPa. The vertical decrease of θ_{se} during the MCS events indicates an instable atmosphere, which favours the initiation and development of convection. The difference in θ_{se} anomalies between the MCS and non-MCS events (Figure 12d) further demonstrates that the θ_{se} during the MCS events is higher than that

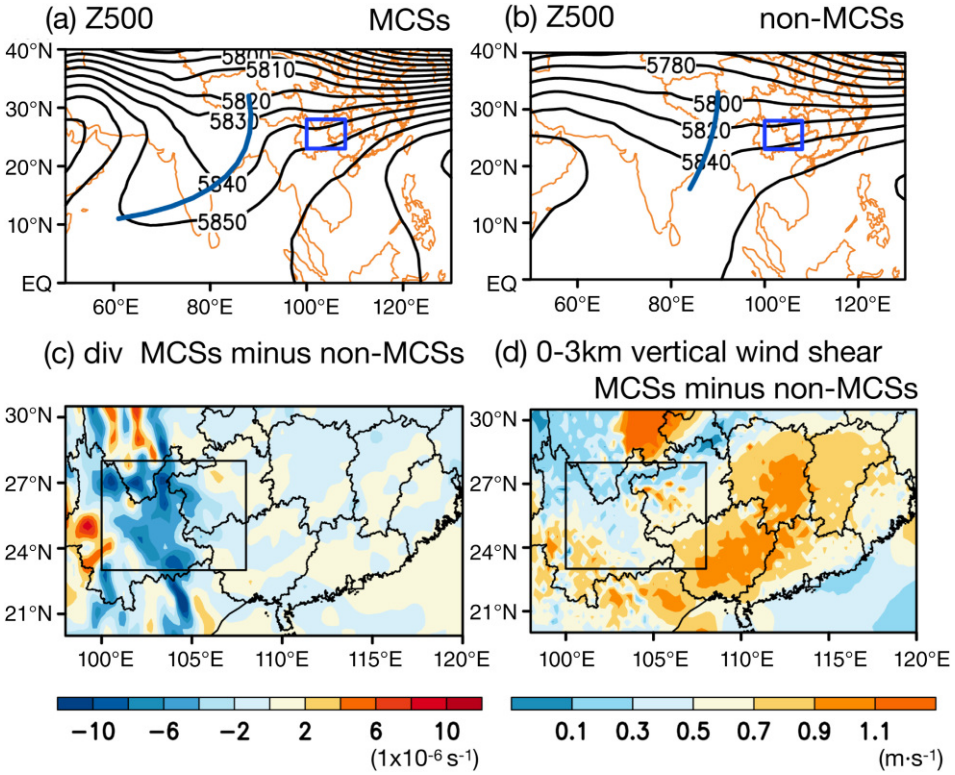

FIGURE 11 Composite geopotential height (contour; units: gpm) at 500 hPa for (a) MCS and (b) non-MCS events. (c) The difference in divergence (shading; units: 1×10^{-6} s^{-1}) at 700 hPa and (d) in 0–3 km vertical shear of wind anomalies (shading; units: m·s^{-1}) between MCSs and non-MCSs [Colour figure can be viewed at wileyonlinelibrary.com]

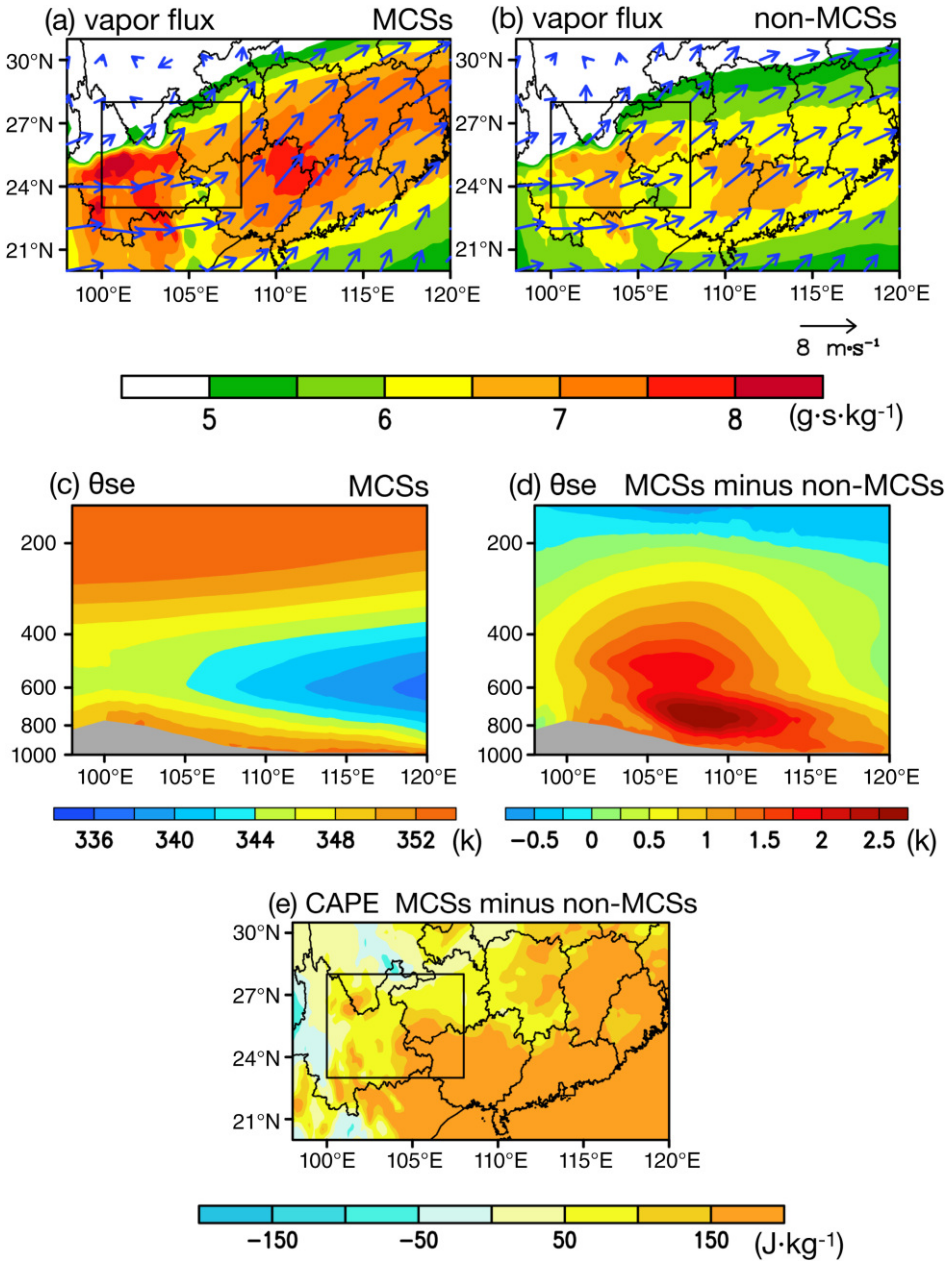

FIGURE 12 Composite water vapour flux (shading; units: $g \cdot s \cdot kg^{-1}$) and wind field (vector; units: $m \cdot s^{-1}$) at 700 hPa for (a) MCS and (b) non-MCS events. (c) Composite height-longitudinal cross sections of potential pseudo-equivalent temperature (θ_{se}) (shading; units: K) averaged over 23°–28°N for MCS events and (d) difference in θ_{se} anomalies (shading; units: K) between MCSs and non-MCSs. The grey shading is terrain height (shading; units: m) averaged over 23°–28°N. (e) The difference in CAPE (shading; units: $J \cdot kg^{-1}$) between MCSs and non-MCSs [Colour figure can be viewed at wileyonlinelibrary.com]

during the non-MCS events from the MCSs' formation area to its downstream (~0–3.0 K). The results above suggest the MCSs are easy to generate and develop if the air mass above the YGP has larger thermal energy to ascend. Similarly, the difference in CAPE during the MCSs events from the non-MCSs events is also positive over the YGP and its downstream regions (Figure 12e).

As mentioned in section 3.2, the number of MCSs generated over the YGP is varied among months. Such monthly variations are attributed to the seasonal difference in background circulation around the YGP. Figure 13 presents the climatological monthly mean geopotential height from April to August. The notable 500-hPa troughs over South Asia are observed in June–August rather than April. That can partly explain why the MCSs formed in April happen least. Besides that, as shown in Figure 14, stronger divergence at 700 hPa over YGP in April–May also cause the minimum amounts of MCSs in these months. In addition, the strong divergence in April–May may result from the strong 700-hPa wind velocity cores occurring over the downstream of the maximum divergence centres (Figure 14a,b).

In addition to the dynamic conditions demonstrated above, the thermodynamic environmental conditions also vary from April to August. As shown in Figure 15, the averaged surface temperature and CAPE over the YGP are lowest in April (~16.0°C; ~138.8 $J \cdot kg^{-1}$) and reach highest in July (~20.7°C; ~430.0 $J \cdot kg^{-1}$). The water vapour flux at

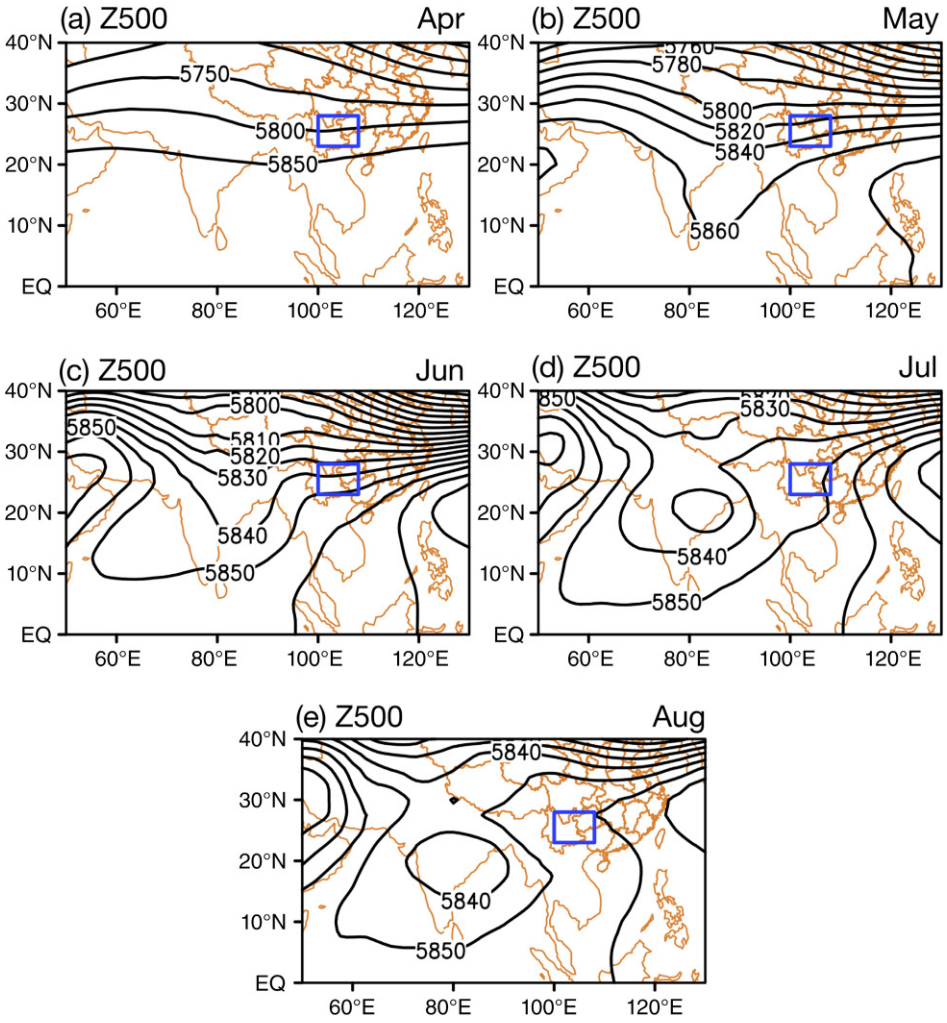

FIGURE 13 Composite geopotential height (contour; units: gpm) at 500 hPa from April to August [Colour figure can be viewed at wileyonlinelibrary.com]

700 hPa reaches a peak in June (~6.3 g·s·kg^{-1}), consistent with the peak of the MCS numbers. If we only consider the monthly variation of dynamic factors and CAPE, the MCSs are supposed to occur most frequently in July or August rather than June. Therefore, the monthly variations of water vapour flux play an important role in the monthly variations of occurrence of the MCSs. In sum, the generation and development of MCSs are caused by the combination of dynamics and thermodynamics. The abundant moisture supply is vital for the generation of MCSs in June, whereas the high CAPE and dynamic forcing are favourable to MCSs in July.

4.2 | The comparison in environmental conditions between EMT and NDT events

Next, we investigate the factors driving the MCSs to vacate the YGP from dynamic and thermodynamic perspectives by compositing the EMT and NDT events based on the hourly dataset. First, much stronger 500-hPa westerly wind over the YGP and its downstream is found during the EMT events than the NDTs (Figure 16a,b). The maximum westerly wind velocity core (~9 m·s^{-1}) is located downstream. The strong steering flow favours the MCSs to vacate the YGP.

As shown in Figure 16c,d, the EMTs have stronger 0–3 km vertical wind shear than the NDTs, especially for downstream regions, which is beneficial to the maintenance and evolution of the convection (Schumacher and Johnson, 2005; DeLonge *et al.*, 2010). Therefore, the lifespans of EMTs are longer with stronger vertical wind shear downstream.

The difference in water vapour flux between the two types of MCSs is also notable (Figure 17a,b). The water vapour flux of EMTs over the downstream (~8.0–10.0 g·s·kg^{-1}) is obviously larger than that of NDTs (~6.0–8.0 g·s·kg^{-1}). The strong water vapour transportation to downstream favours the eastward propagation of MCSs. On the contrary, the vapour flux of NDTs is weaker and mainly distributed in the western area of the YGP. Abundant moisture favours the initiation and development of the convection, and large vapour flux over the downstream is favourable for convection to

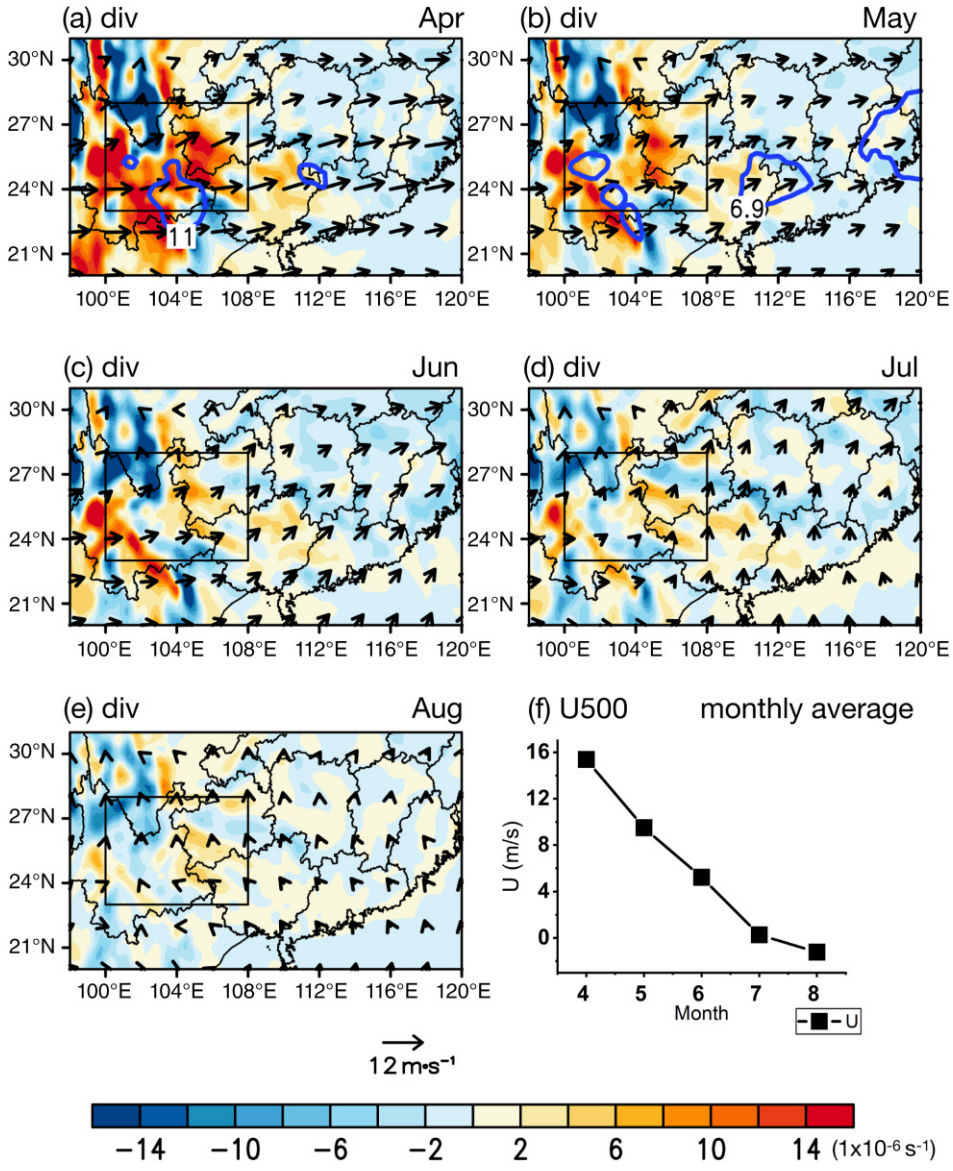

FIGURE 14 (a–e) Composite divergence (shading; units: 1×10^{-6} s^{-1}) at 700 hPa and wind field (vector; units: $m \cdot s^{-1}$) at 500 hPa from April to August. The contour in panels (a, b) represents maximum wind velocity at 700 hPa. (f) The mean wind velocity of zonal wind at 500 hPa averaged in the area of the YGP (23°–28°N, 100°–108°E) from April to August [Colour figure can be viewed at wileyonlinelibrary.com]

move eastward and develop (Yang *et al.*, 2020). Furthermore, the relative vorticity of EMTs is about 2×10^{-5} $m \cdot s^{-1}$ greater than that of NDTs in the eastern section of the YGP and the downstream (Figure 17a,b). In sum, the abundant water vapour accompanied with the strong vorticity over the YGP and its downstream area provide favourable conditions for MCSs to move off the YGP and persist for a long time.

As shown in Figure 17c, the θ_{se} during the EMT events decreases significantly as the latitude increase below 600 hPa, especially downstream. It also should be noted in Figure 17d that the maximum centre of the difference in θ_{se} anomalies between EMTs and NDTs expands from the eastern YGP to the downstream, while the pattern in the western YGP is opposite. The CAPE for the EMT events is also larger than the NDTs downstream, while the CAPE for EMTs is lower than NDTs over the YGP (Figure 17e), which is similar to the distribution of θ_{se}. Therefore, the maximum instability distributed over the YGP is favourable for MCSs to initiate rather than move eastward. By contrast, the larger thermodynamic conditions over the downstream can drive the MCSs to move eastward and expand the duration after vacating the YGP.

Overall, the MCSs are inclined to vacate the YGP and have longer lifespans when both the dynamic and thermodynamic conditions are favourable, especially over the downstream. For the monthly variation, the decline in the EMT proportion from April to August might be caused by the northern march of westerlies. Both 500-hPa westerly wind (Figure 14) and low-level vertical wind shear (Figure 18) around the YGP and its downstream are strongest in April, which facilitates the MCSs to move eastward. And the differences among each month explain

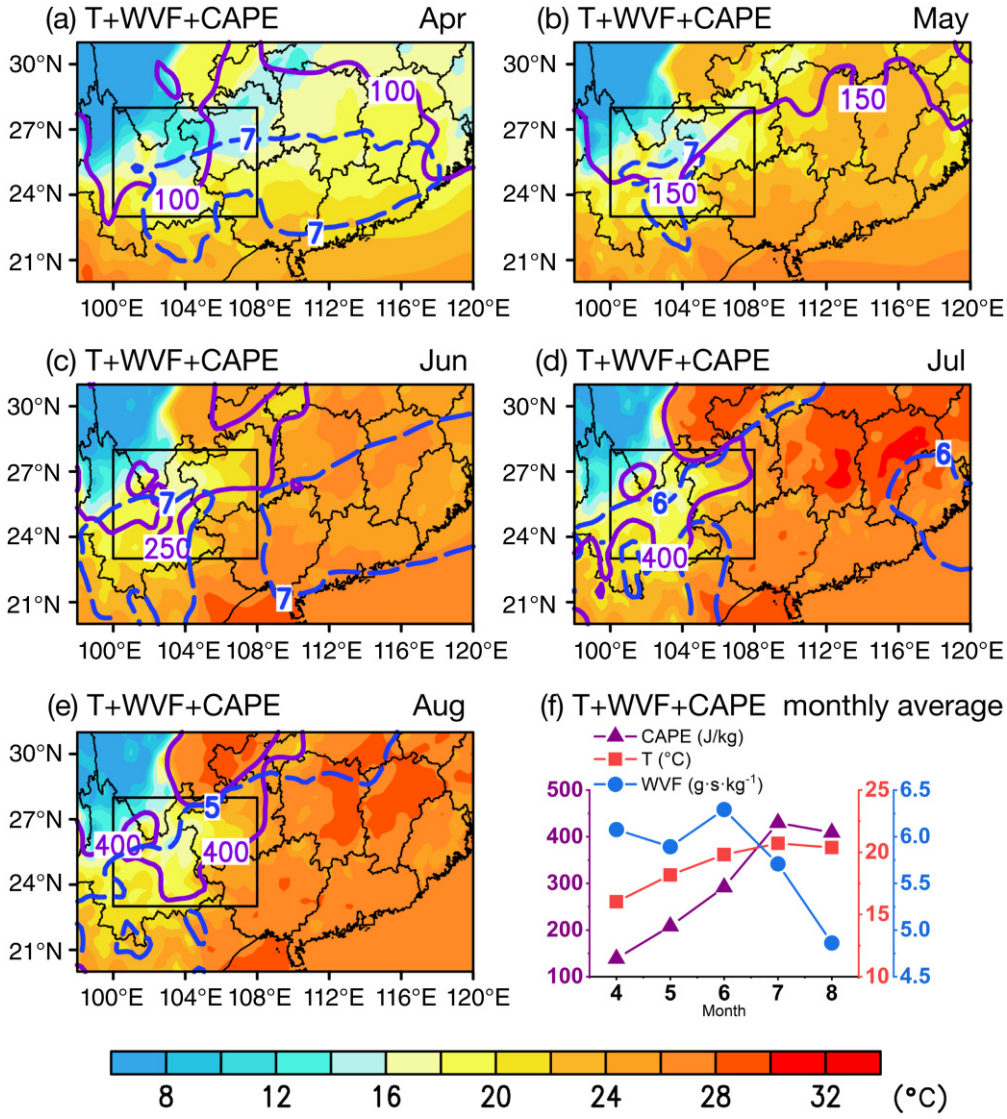

FIGURE 15 (a–e) Composite surface temperature (shading; units: °C), CAPE (contour; units: $J \cdot kg^{-1}$), and water vapour flux (dashed contour; units: $g \cdot s \cdot kg^{-1}$) from April to August. (f) The monthly variations of surface temperature, CAPE, and water vapour flux at 700 hPa averaged in the area of the YGP (23°–28°N, 100°–108°E) from April to August [Colour figure can be viewed at wileyonlinelibrary.com]

the monthly variations in the ratios of EMTs and NDTs from April to August (Figure 9b).

5 | COMPARISONS OF MCSS GENERATED OVER THE YGP AND TP

The MCSs generated over the YGP (MCSs-YGP) exhibit similarities and differences from those generated over the TP (MCSs-TP) due to the different terrain and environments (Fu *et al.*, 2013; Hu *et al.*, 2016; Mai *et al.*, 2021; Zhang *et al.*, 2021). Considering that the different tracking algorithms and criteria of MCSs could make the comparison inaccurate, we compare the features of the MCSs-YGP with MCSs-TP studied by Mai *et al.* (2021), as we use the same data and methodology.

The numbers of MCSs-YGP reach the peak in June, which is about 1 month earlier than the peak of the MCSs-TP (July). The monthly variation of the MCSs-YGP number in April–August is similar to that of the MCSs-YGP in May–September (Figure 19). Such variations are related to the northward march of the summer monsoon. Therefore, we regard April–August (May–September) as the warm season of the MCSs-YGP (MCSs-TP) in the present study. The total amount of MCSs-YGP (~102.5) per warm season is about 1/6 of that of MCSs-TP (~609.6).

The diurnal cycle of MCSs-YGP is similar to that of MCSs-TP. The occurrence number of both MCSs-YGP and MCSs-TP increases rapidly from 1200 LST and peaks at 1400–1600 LST when the strongest surface longwave radiation appears; then the occurrence number decreases until the next day.

The proportion of EMTs over the YGP (~13.1%) in the warm seasons is higher than the TP (~6.6%). The higher ratios of EMT over the YGP occur each month except for August. The more abundant moisture downstream may be one of the possible reasons for the higher

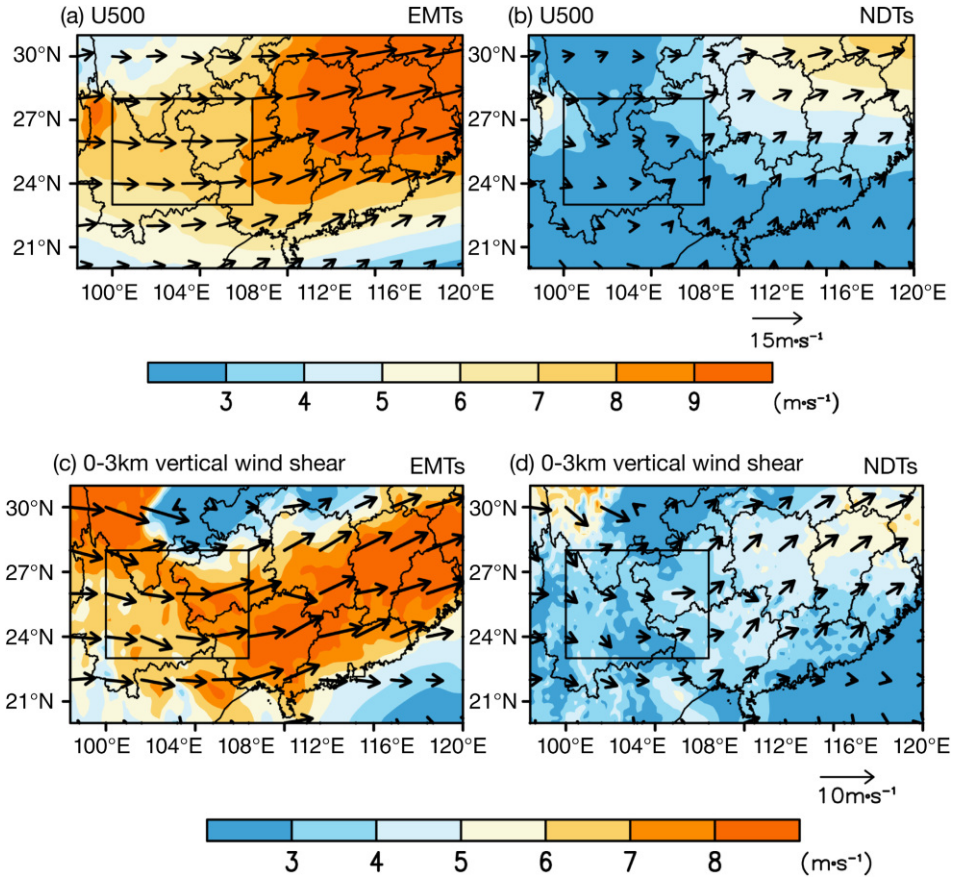

FIGURE 16 Composite wind field (vector; units: $m \cdot s^{-1}$) and wind velocity (shading; units: $m \cdot s^{-1}$) at 500 hPa for (a) EMT and (b) NDT events. Composite 0–3 km vertical wind shear field (vector; units: $m \cdot s^{-1}$) and vertical wind shear velocity (shading; units: $m \cdot s^{-1}$) for (c) EMTs and (d) NDTs events [Colour figure can be viewed at wileyonlinelibrary.com]

eastward moving proportion of the MCSs-YGP. Another possible reason might be stronger steering flow within the YGP region and its downstream from April to July. As the westerly jet marches northward, the steering flow around the YGP gets weaker, which might cause a lower ratio of EMTs over the YGP than the TP in August. In addition, MCSs tend to stay in the TP due to the relatively larger area of the TP.

The MCSs-YGP usually have longer lifespans than MCSs-TP. For NDTs, the mean lifespan of MCSs-YGP (MCSs-TP) in the warm seasons is ~7.6 hr (5.5 hr), while the average lifespan of EMTs is ~16.5 hr (~11.9 hr) over the YGP (TP). The lifespan of EMTs over the YGP peaks in June (~21.3 hr), whereas that over the TP peaks in July (~15.1 hr). Such difference in peak time may result from the northward march of the monsoon. Moreover, the long-lived MCSs of the YGP account for a larger percentage of their total amount compared to TP. About 18.6% of EMTs over the YGP last longer than 24 hr, but only ~8.4% of those over the TP do so. Meanwhile, the NDTs of the YGP with a lifespan longer than 6 hr make up around 39.0%, which is larger than that of the TP (~25.0%). The possible reason for the difference in lifespan may be that the more abundant moisture over the YGP and its downstream regions favour the YGP MCSs to persist for a longer time compared to the TP.

6 | CONCLUSION

Based on hourly TBB geostationary satellites data, 1845 MCSs generated over the YGP are detected during the warm seasons (April–August) in 2000–2018 (except for 2005). Using an automatic tracking algorithm (Li, 2010) accompanied by manual corrections, we investigate the characteristics of MCSs formed over the YGP and their relevant mechanisms in the present study.

The MCSs are grouped as the eastward moving type (EMT) and non-eastward moving/dissipating type (NDT), showing different features. The number of the NDTs (~89 per year, ~86.9%) is larger than the EMTs (~13 per year, ~13.1%). However, the EMTs have a longer mean lifespan (~16.5 hr) than the NDTs (~7.6 hr). In addition, the EMTs are mainly initiated and active in the eastern flank of the YGP. By contrast, the NDTs form over the YGP evenly and are active mainly in the central YGP. The maximum EMT- and NDT-related precipitation centres are consistent with the activity frequency centres of EMTs and NDTs. The EMT-related precipitation has a notable influence on the downstream regions, while the NDTs mainly produce precipitation over the YGP. Further classification of the EMTs indicates that the ratio of the eastward moving EMTs is the highest (~77.6%), followed by the southeastward moving EMTs (~13.3%) and

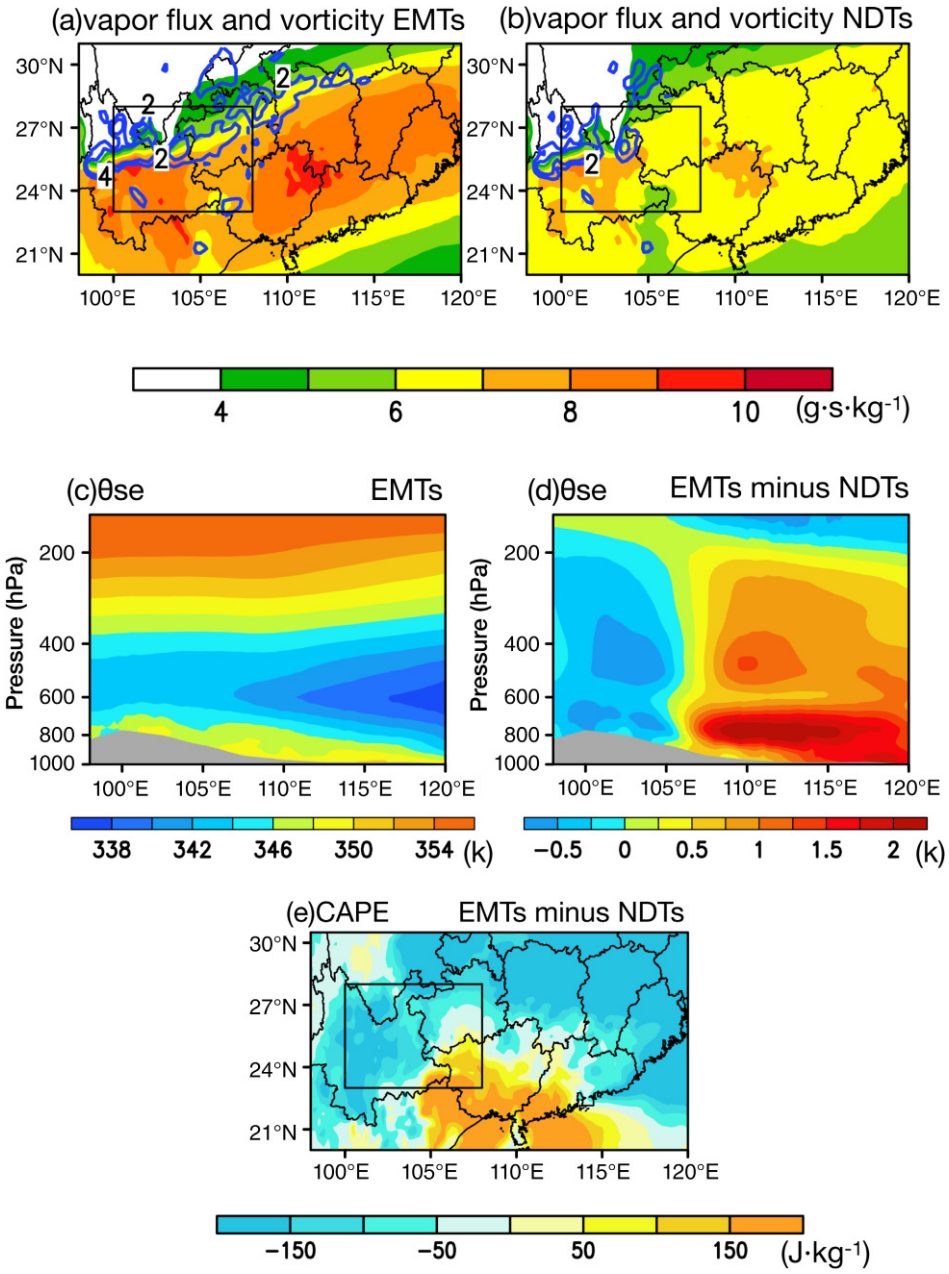

FIGURE 17 Composite water vapour flux (shading; units: $g{\cdot}s{\cdot}kg^{-1}$) and relative vorticity (contour; units:$1 \times 10^{-5}\ s^{-1}$) at 700 hPa for (a) EMT and (b) NDT events. (c) Composite height-longitudinal cross sections of θ_{se} (shading; units: K) averaged over 23°–28°N for EMT events and (d) difference in θ_{se} anomalies (shading; units: K) between EMTs and NDTs. The grey shading is terrain height (shading; units: m) averaged over 23°–28°N. (e) The difference in CAPE (shading; units: $J{\cdot}kg^{-1}$) between EMTs and NDTs [Colour figure can be viewed at wileyonlinelibrary.com]

northeastward moving EMTs (~9.1%). The longer-lifespan EMTs (those that persist for at least 6 hr in their lifespans and last for at least 3 hr after vacating the YGP) account for the highest proportion of all EMTs (~71.0%).

The number of MCSs generated over the YGP varies each year in the warm seasons, from 74 in 2011 to 133 in 2000. In addition, the highest ratio of EMTs is in 2007 (~22.6%), whereas the lowest one is in 2013 (~5.7%). In the studied period, the occurrence frequency of MCSs and their other features (e.g., lifespans, ratio of EMTs) do not show significant increasing or decreasing trends. The monthly variations of the MCSs are also evident. In June–July, the number of MCSs accounts for more than 60.0% of total MCS numbers in the warm seasons, while that in April only makes up 4.4%. However, the proportion of EMTs in April reaches the highest (~50.0%). Compared to April, the environment in June–July favours the occurrence of MCSs. The abundant moisture supply plays a vital role in the generation and development of MCSs in June, whereas the high CAPE and dynamic forcing are favourable to MCSs in July. By contrast, the environment in April is conducive to the eastward propagation of the MCSs with the stronger mid-level westerlies and low-level wind shear over the downstream.

Besides the interannual and monthly variations, the diurnal variations of MCSs are also pronounced. The diurnal variations of the EMTs and NDTs show apparent differences. The generation peak of the EMTs (~1600 LST) is

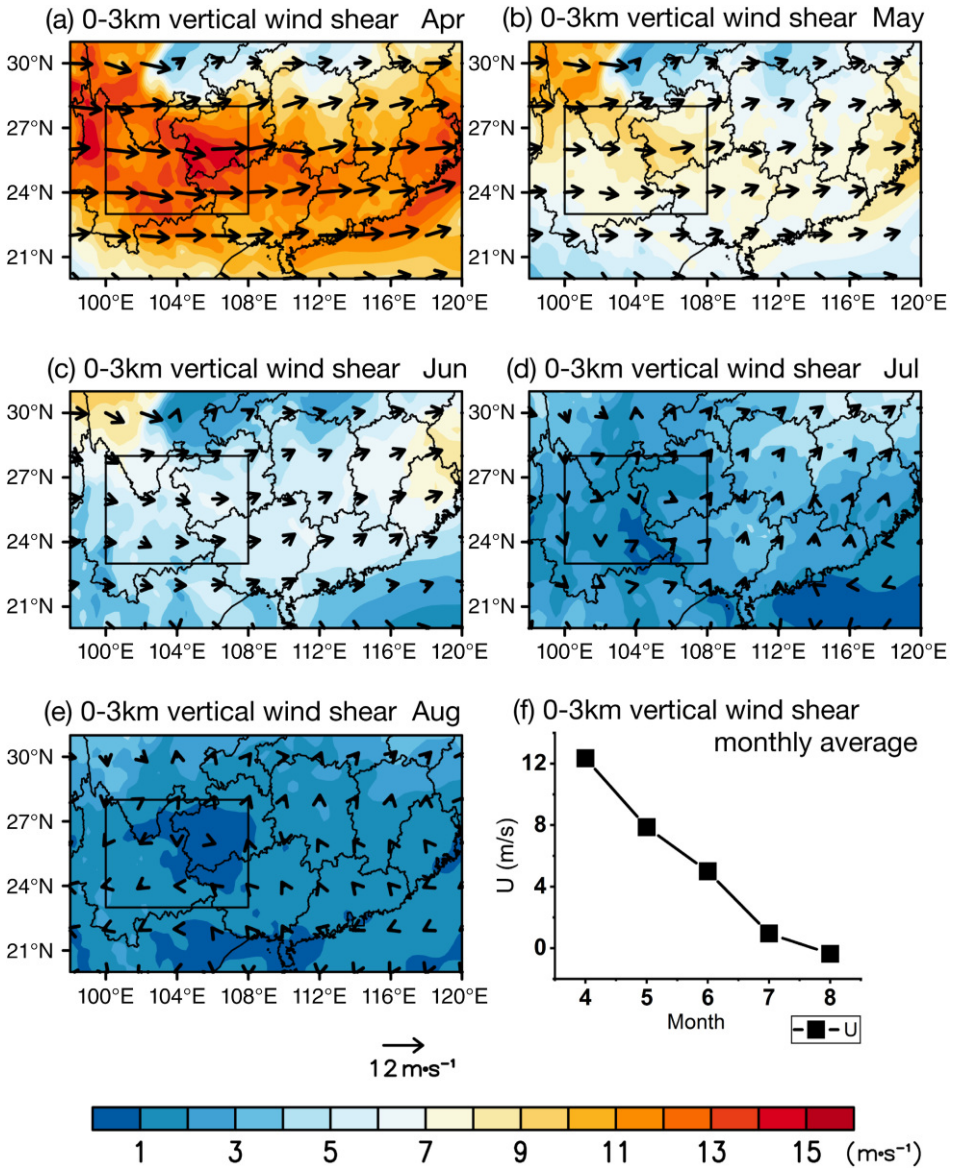

FIGURE 18 (a–e) Composite 0–3 km vertical wind shear field (vector; units: $m \cdot s^{-1}$) and vertical wind shear velocity (shading; units: $m \cdot s^{-1}$) from April to August. Panel (f) shows the mean wind velocity of 0–3 km vertical zonal wind shear averaged in the area of the YGP (23°–28°N, 100°–108°E) from April to August [Colour figure can be viewed at wileyonlinelibrary.com]

about 1 hr later than that of NDTs (~1500 LST). The EMTs have two maturation peaks, in the late afternoon and early morning, whereas the maturation peak of the NDTs occurs only in the late afternoon. The NDTs mainly vanish over the YGP at around 1900–2100 LST, while the EMTs can dissipate at various timing and locations due to their long lifespans when the environment becomes unfavourable.

We further examine the environmental conditions conducive to the generation and development of MCSs by comparing the MCSs and non-MCS events. The combinations of middle-tropospheric troughs over South Asia and strong low-level vertical wind shear and water vapour flux over both YGP and its downstream regions are conducive to convective organization and development. What's more, the EMTs are more active in an instable environment downstream with strong mid-level westerlies and low-level vertical wind shear. The MCSs tend to form when dynamic and thermodynamic conditions are favourable over the YGP, whereas the MCSs are inclined to vacate the YGP and have longer lifespans if favourable environmental conditions occur downstream.

In addition, we compare the MCSs generated over the YGP and TP. The total amount of MCSs-YGP per warm season is about 1/6 of that of MCSs-TP. However, the ratio of EMTs over the YGP is higher than the TP. Moreover, the MCSs-YGP usually have longer lifespans than MCSs-TP, and the lifespans of NDTs are shorter than that of EMTs for both MCSs-YGP and MCSs-TP.

Several methods are adopted to identify and track MCSs in the previous studies, including surface precipitation (Houze, 2004; Li *et al.*, 2020), cloud-top brightness temperature (Yang *et al.*, 2015; Chen *et al.*, 2019; Mai *et al.*, 2021), and composite reflectivity Doppler radar data (Zheng *et al.*, 2013). In the present study, we only

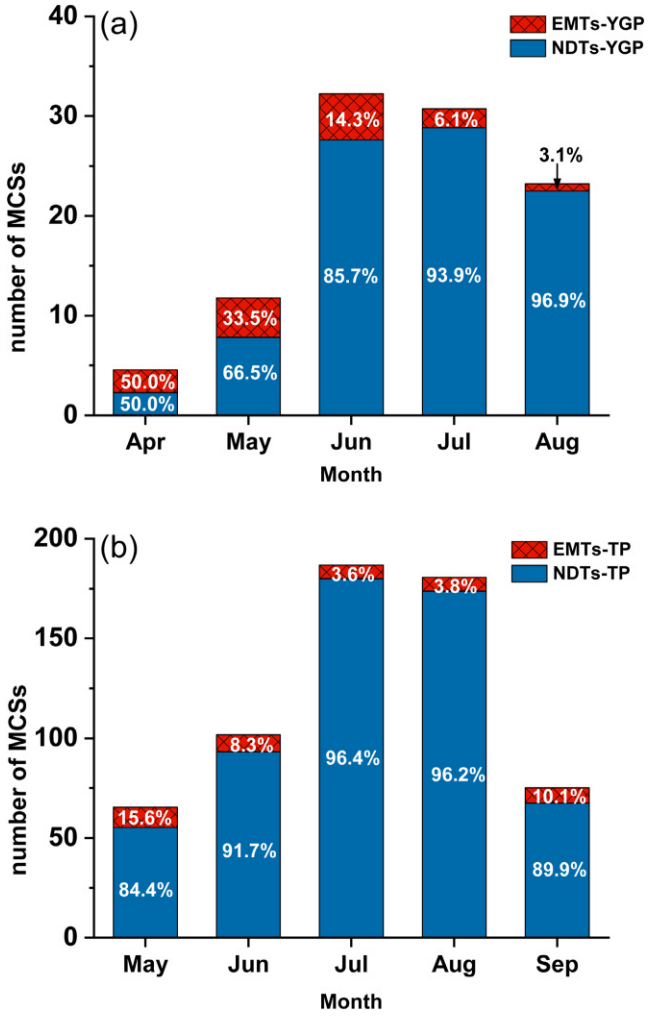

FIGURE 19 The mean occurrence numbers of (a) MCSs-YGP in April–August and (b) MCSs-TP in May–September. The contribution ratio (%) of EMTs and NDTs to the total number of MCSs in each month [Colour figure can be viewed at wileyonlinelibrary.com]

use the cloud-top properties to track MCSs over the YGP. For future studies, we will consider more combined atmospheric variables to improve the identification and tracking method. Also, the TBB thresholds reflecting convective activity in different regions of China vary, although the difference is not large (Li, 2010). Therefore, more TBB thresholds to detect the MCSs over YGP would be examined. In addition, further studies are required on the mechanisms of how EMTs induce intense precipitation over the downstream areas.

ACKNOWLEDGEMENTS

We would like to thank the European Center for Medium-Range Weather Forecasts for the ERA-5 reanalysis data and National Oceanic and Atmospheric Administration for CMORPH high-resolution precipitation data. We also appreciate the data of TBB observed by geostationary satellites provided by Japan Meteorological (http://weather.is.kochi-u.ac.jp/archive-e.html). This study was supported by the Guangdong Major Project of Basic and Applied Basic Research (2020B0301030004), the National Natural Science Foundation of China (Grant Nos. 42122033, 41875055, and 42075006), and Guangzhou Science and Technology Plan Projects (202002030346).

AUTHOR CONTRIBUTIONS

Yuanjing Guo: Conceptualization; data curation; formal analysis; investigation; methodology; software; visualization; writing – original draft. **Yu Du:** Conceptualization; funding acquisition; investigation; methodology; supervision; validation; writing – review and editing. **Riyu Lu:** Formal analysis; investigation; methodology; supervision; validation; writing – review and editing. **Xinxian Feng:** Investigation; software; validation; writing – review and editing. **Jun Li:** Methodology; software; writing – review and editing. **Yuanchun Zhang:** Methodology; validation; writing – review and editing. **Zi Mai:** Software; validation; writing – review and editing.

ORCID

Yuanjing Guo https://orcid.org/0000-0001-8878-6172
Yu Du https://orcid.org/0000-0001-8828-5431
Xinxian Feng https://orcid.org/0000-0003-2441-1608

REFERENCES

Ai, Y., Li, W., Meng, Z. and Li, J. (2016) Life cycle characteristics of MCSs in middle East China tracked by geostationary satellite and precipitation estimates. *Monthly Weather Review*, 144, 2517–2530. https://doi.org/10.1175/MWR-D-15-0197.1.

Augustine, J.A. and Caracena, F. (1994) Lower-tropospheric precursors to nocturnal MCS development over the central United States. *Weather Forecasting*, 9, 116–135. https://doi.org/10.1175/1520-0434(1994)009<0116:Ltptnm>2.0.Co;2.

Augustine, J.A. and Howard, K.W. (1991) Mesoscale convective complexes over the United States during 1985. *Monthly Weather Review*, 116, 685–701. https://doi.org/10.1175/1520-0493(1988)116<0685:Mccotu>2.0.Co;2.

Chen, D., Guo, J., Yao, D., Feng, Z. and Lin, Y. (2020) Elucidating the life cycle of warm-season mesoscale convective systems in eastern China from the Himawari-8 geostationary satellite. *Remote Sensing*, 12, 2307. https://doi.org/10.3390/rs12142307.

Chen, D., Guo, J., Yao, D., Lin, Y., Zhao, C., Min, M., Xu, H., Liu, L., Huang, X., Chen, T. and Zhai, P. (2019) Mesoscale convective systems in the Asian monsoon region from advanced Himawari imager: algorithms and preliminary results. *Journal of Geophysical Research: Atmospheres*, 124, 2210–2234. https://doi.org/10.1029/2018JD029707.

Chen, Q., Fan, J., Hagos, S., Gustafson, W.I. and Berg, L.K. (2015) Roles of wind shear at different vertical levels: cloud system organization and properties. *Journal of Geophysical Research: Atmospheres*, 120, 6551–6574. https://doi.org/10.1002/2015JD023253.

Dai, A. (2001) Global precipitation and thunderstorm frequencies. Part II: Diurnal variations. *Journal of Climate*, 14, 1112–1128.

DeLonge, M.S., Fuentes, J.D., Chan, S., Kucera, p.A., Joseph, E., Gaye, A.T. and Daouda, B. (2010) Attributes of mesoscale convective systems at the land-ocean transition in Senegal during NASA African monsoon multidisciplinary analyses 2006. *Journal of Geophysical Research: Atmospheres*, 115, 213. https://doi.org/10.1029/2009JD012518.

Doswell, C.A., Brooks, H.E. and Maddox, R.A. (1996) Flash flood forecasting: an ingredients-based methodology. *Weather Forecasting*, 11, 560–581. https://doi.org/10.1175/1520-0434(1996)011<0560:Fffaib>2.0.Co;2.

Du, Y., Zhang, Q., Chen, Y., Zhao, Y. and Wang, X. (2014) Numerical simulations of spatial distributions and diurnal variations of low-level jets in China during early summer. *Journal of Climate*, 27, 5747–5767.

Du, Y. and Chen, G.X. (2019) Heavy Rainfalls Associated with Double Low-level Jets over Southern China. Part II: Convection initiation. *Mon. Wea. Rev.* 147, 543–565. https://doi.org/10.1175/MWR-D-18-0102.1

Duan, X., Zhang, M. and Xu, M. (2004) Temporal and spatial distribution of mesoscale convective systems over Yunnan and its surrounding areas. *Acta Meteorologica Sinica*, 62, 243–257 (in Chinese).

Feng, Z., Dong, X., Xi, B., McFarlane, S.A., Kennedy, A., Lin, B. and Minnis, P. (2012) Life cycle of midlatitude deep convective systems in a Lagrangian framework. *Journal of Geophysical Research*, 117, 201. https://doi.org/10.1029/2012JD018362.

Feng, Z., Houze, R.A., Leung, L.R., Song, F., Hardin, J.C., Wang, J., Gustafson, W.I. and Homeyer, C.R. (2019) Spatiotemporal characteristics and large-scale environments of mesoscale convective systems east of the Rocky Mountains. *Journal of Climate*, 32, 7303–7328. https://doi.org/10.1175/jcli-d-19-0137.1.

Feng, Z., Leung, L.R., Hagos, S., Houze, R.A., Burleyson, C.D. and Balaguru, K. (2016) More frequent intense and long-lived storms dominate the springtime trend in central US rainfall. *Nature Communications*, 7, 13429. https://doi.org/10.1038/ncomms13429.

Feng, Z., Leung, L.R., Liu, N., Wang, J., Houze, R.A., Li, J., Hardin, J.C., Chen, D. and Guo, J. (2021) A global high-resolution mesoscale convective system database using satellite-derived cloud tops, surface precipitation, and tracking. *Journal of Geophysical Research: Atmospheres*, 126, e2020JD034202. https://doi.org/10.1029/2020JD034202.

Fu, S.M., Sun, J., Zhao, S., Li, W. and Li, B. (2011) A study of the impacts of the eastward propagation of convective cloud systems over the Tibetan Plateau on the rainfall of the Yangtze–Huai River basin. *Acta Meteorologica Sinica*, 69, 581–600 (in Chinese).

Fu, W., Wang, D., Yin, H., Yin, J. and Li, J. (2013) Contrast analysis on statistical characteristic of MCSs over Qinghai–Xizang Plateau and East Asia in warm season. *Plateau Meteorology*, 32, 929–943 (in Chinese).

Haberlie, A.M. and Ashley, W.S. (2019) A radar-based climatology of mesoscale convective systems in the United States. *Journal of Climate*, 32, 1591–1606. https://doi.org/10.1175/JCLI-D-18-0559.1.

Hersbach, H., Bell, B., Berrisford, P., Hirahara, S., Horányi, A., Muñoz-Sabater, J., Nicolas, J., Peubey, C., Radu, R., Schepers, D., Simmons, A., Soci, C., Abdalla, S., Abellan, X., Balsamo, G., Bechtold, P., Biavati, G., Bidlot, J., Bonavita, M., Chiara, G., Dahlgren, P., Dee, D., Diamantakis, M., Dragani, R., Flemming, J., Forbes, R., Fuentes, M., Geer, A., Haimberger, L., Healy, S., Hogan, R.J., Hólm, E., Janisková, M., Keeley, S., Laloyaux, P., Lopez, P., Lupu, C., Radnoti, G., Rosnay, P., Rozum, I., Vamborg, F., Villaume, S. and Thépaut, J.N. (2020) The ERA5 global reanalysis. *Quarterly Journal of the Royal Meteorological Society*, 146, 1999–2049. https://doi.org/10.1002/qj.3803.

Holton, J.R. (2004) *An Introduction to Dynamic Meteorology*, 4th edition. San Diego, CA: Academic Press.

Houze, R.A. (2004) Mesoscale convective systems. *Reviews of Geophysics*, 42, RG4003. https://doi.org/10.1029/2004RG000150.

Houze, R.A., Smull, B.F. and Dodge, P. (1990) Mesoscale organization of springtime rainstorms in Oklahoma. *Monthly Weather Review*, 118, 613–654. https://doi.org/10.1175/1520-0493(1990)118<0613:Moosri>2.0.Co;2.

Hu, L., Deng, D., Gao, S. and Xu, X. (2016) The seasonal variation of Tibetan convective systems: satellite observation. *Journal of Geophysical Research: Atmospheres*, 121, 5512–5525. https://doi.org/10.1002/2015JD024390.

Hu, M.K. (1962) Visual pattern recognition by moment invariant. *IEEE Transactions on Information Theory*, 28, 179–187.

Jiang, J., Xiang, X. and Fan, M. (1996) The spatial and temporal distributions of severe mesoscale convective systems over Tibetan Plateau in summer. *Journal of Applied Meteorological Science*, 7, 473–478 (in Chinese).

Joyce, R.J., Janowiak, J.E., Arkin, p.A. and Xie, P. (2004) CMORPH: a method that produces global precipitation estimates from passive microwave and infrared data at high spatial and temporal resolution. *Journal of Hydrometeorology*, 5, 487–503. https://doi.org/10.1175/1525-7541(2004)005<0487:Camtpg>2.0.Co;2.

Laing, A.G. and Fritsch, J.M. (1993) Mesoscale convective complexes in Africa. *Monthly Weather Review*, 121, 2254–2263. https://doi.org/10.1175/1520-0493(1993)121<2254:Mccia>2.0.Co;2.

Laing, A.G. and Michael, F.J. (1997) The global population of mesoscale convective complexes. *Quarterly Journal of the Royal Meteorological Society*, 123, 389–405. https://doi.org/10.1002/qj.49712353807.

Li, J. (2010) *Study on the characteristics of the mesoscale convective cloud clusters occurred in east asia during warm seasons*. PhD dissertation, Institute of Atmospheric Physics, Chinese Academy of Sciences, Beijing (in Chinese).

Li, J., Wang, B. and Wang, D.H. (2012) The characteristics of mesoscale convective systems (MCSs) over East Asia in warm seasons. *Atmospheric and Oceanic Science Letters*, 5, 102–107. https://doi.org/10.1080/16742834.2012.11446973.

Li, J.Y., Shen, X.Y., Wang, D.H. and Li, J. (2015) Distribution and characteristics of the MCS over south China during the spring and summer of 2008. *Journal of Tropical Meteorology*, 31, 475–485 (in Chinese). https://doi.org/10.16032/j.issn.1004-4965.2015.04.005.

Li, P., Moseley, C., Prein, A.F., Chen, H., Li, J., Furtado, K. and Zhou, T. (2020) Mesoscale convective system precipitation characteristics over East Asia. Part I: regional differences and seasonal variations. *Journal of Climate*, 33, 9271–9286. https://doi.org/10.1175/jcli-d-20-0072.1.

Liu, N., Leung, L.R. and Feng, Z. (2021) Global mesoscale convective system latent heating characteristics from GPM retrievals

and an MCS tracking dataset. *Journal of Climate*, 34, 8599–8613. https://doi.org/10.1175/JCLI-D-20-0997.1.

Lu, X., Ma, J. and Wu, C. (1987) A shape analytical method of two dimensional objects. *Journal on Communications*, 8, 61–67 (in Chinese).

Ma, Y., Wang, X. and Tao, Z. (1997) Geographic distribution and life cycle of mesoscale convective system in China and vicinity. *Progress in Natural Science*, 7, 701–706.

Maddox, R.A. (1980) Mesoscale convective complexes. *Bulletin of the American Meteorological Society*, 61, 1374–1387. https://doi.org/10.1175/1520-0477(1980)061<1374:Mcc>2.0.Co;2.

Maddox, R.A. (1983) Large-scale meteorological conditions associated with midlatitude, mesoscale convective complexes. *Monthly Weather Review*, 111, 1475–1493. https://doi.org/10.1175/1520-0493(1983)111<1475:Lsmcaw>2.0.Co;2.

Mai, Z., Fu, S.M., Sun, J.H., Hu, L. and Wang, X.M. (2021) Key statistical characteristics of the mesoscale convective systems generated over the Tibetan Plateau and their relationship to precipitation and southwest vortices. *International Journal of Climatology*, 41, 875–896. https://doi.org/10.1002/joc.6735.

Markowski, P. and Richardson, Y. (2010) *Mesoscale Meteorology in Midlatitudes*. West Succex, UK: Wiley John Wiley & Sons, Ltd. https://doi.org/10.1002/9780470682104.

Mathon, V., Diedhiou, A. and Laurent, H. (2002) Relationship between easterly waves and mesoscale convective systems over the Sahel. *Geophysical Research Letters*, 29, 1216. https://doi.org/10.1029/2001GL014371.

Mathon, V. and Laurent, H. (2001) Life cycle of Sahelian mesoscale convective cloud systems. *Quarterly Journal of the Royal Meteorological Society*, 127, 377–406. https://doi.org/10.1002/qj.49712757208.

Moncrieff, M.W. (1992) Organized convective systems: archetypal dynamical models, mass and momentum flux theory, and parametrization. *Quarterly Journal of the Royal Meteorological Society*, 118, 819–850. https://doi.org/10.1002/qj.49711850703.

Murata, H., Takahashi, M. and Kosaka, Y. (2015) VIS and IR bands of Himawari-8/AHI compatible with those of MTSAT2/imager. *Meteorological Satellite Center Technical Note*, 60, 1–18.

Núñez Ocasio, K.M., Evans, J.L. and Young, G.S. (2020) Tracking mesoscale convective systems that are potential candidates for tropical cyclogenesis. *Monthly Weather Review*, 148, 655–669.

Ogungbenro, S.B., Ajayi, V.O. and Adefolalu, D.O. (2016) Mean state and kinematic properties of mesoscale convective systems over West Africa. *Theoretical and Applied Climatology*, 124, 219–227. https://doi.org/10.1007/s00704-015-1412-3.

Parker, M.D. and Johnson, R.H. (2000) Organizational modes of midlatitude mesoscale convective systems. *Monthly Weather Review*, 128, 3413–3436. https://doi.org/10.1175/1520-0493(2001)129<3413:OMOMMC>2.0.CO;2.

Payne, S.W. and McGarry, M.M. (1977) The relationship of satellite inferred convective activity to easterly waves over West Africa and the adjacent ocean during phase III of Gate. *Monthly Weather Review*, 105, 413–420. https://doi.org/10.1175/1520-0493(1977)105<0413:Trosic>2.0.Co;2.

Qi, X. and Zheng, Y. (2009) Distribution and spatiotemporal variations of deep conversation over China and its vicinity during the summer of 2007. *Journal of Applied Meteorological Science*, 20, 286–294 (in Chinese).

Roca, R. and Fiolleau, T. (2020) Extreme precipitation in the tropics is closely associated with long-lived convective systems. *Communications Earth & Environment*, 1, 18. https://doi.org/10.1038/s43247-020-00015-4.

Rotunno, R., Klemp, J.B. and Weisman, M.L. (1988) A theory for strong, long-lived squall lines. *Journal of the Atmospheric Sciences*, 45, 463–485. https://doi.org/10.1175/1520-0469(1988)045<0463:Atfsll>2.0.Co;2.

Salio, P., Nicolini, M. and Zipser, E.J. (2007) Mesoscale convective systems over southeastern South America and their relationship with the South American low-level jet. *Monthly Weather Review*, 135, 1290–1309. https://doi.org/10.1175/mwr3305.1.

Schmetz, J., Pili, P., Tjemkes, S., Just, D., Kerkmann, J., Rota, S. and Ratier, A. (2002) An introduction to Meteosat Second Generation (MSG). *Bulletin of the American Meteorological Society*, 83, 977–992. https://doi.org/10.1175/1520-0477(2002)083<0977:AITMSG>2.3.CO;2.

Schumacher, R.S. and Johnson, R.H. (2005) Organization and environmental properties of extreme-rain-producing mesoscale convective systems. *Monthly Weather Review*, 133, 961–976. https://doi.org/10.1175/mwr2899.1.

Schumacher, R.S. and Rasmussen, K.L. (2020) The formation, character and changing nature of mesoscale convective systems. *Nature Reviews Earth & Environment*, 1, 300–314. https://doi.org/10.1038/s43017-020-0057-7.

Tahara, Y., Ohkawara, N. and Okuyama, A. (2004) Intercalibration of the infrared channels between GMS-5 and GOES-9. *Meteorological Satellite Center Technical Note*, 44, 1–18.

Trier, S.B. and Parsons, D.B. (1993) Evolution of environmental conditions preceding the development of a nocturnal mesoscale convective complex. *Monthly Weather Review*, 121, 1078–1098. https://doi.org/10.1175/1520-0493(1993)121<1078:Eoecpt>2.0.Co;2.

Yang, J., Du, X., Qi, D. and Luo, X. (2015a) MCC survey and rainfall characteristic in East Mountain of Yunnan–Guizhou Plateau. *Plateau Meteorology*, 34, 1249–1260 (in Chinese).

Yang, R., Zhang, Y., Sun, J. and Li, J. (2020) The comparison of statistical features and synoptic circulations between the eastward-propagating and quasi-stationary MCSs during the warm season around the second-step terrain along the middle reaches of the Yangtze River. *Science China: Earth Sciences*, 63, 1209–1222. https://doi.org/10.1007/s11430-018-9385-3.

Zeng, B., Chen, Y. and Li, Z. (2016) Characteristic of precursor environment of mesoscale convective system during summer in central-eastern China. *Plateau Meteorology*, 35, 460–468 (in Chinese).

Zhang, X., Shen, W., Zhuge, X., Yang, S., Chen, Y., Wang, Y., Chen, T. and Zhang, S. (2021) Statistical characteristics of mesoscale convective systems initiated over the Tibetan Plateau in Suin the late afternoonmmer by Fengyun satellite and precipitation estimates. *Remote Sensing*, 13, 1652. https://doi.org/10.3390/rs13091652.

Zhao, M. (2022) A study of AR-, TS-, and MCS-associated precipitation and extreme precipitation in present and warmer climates. *Journal of Climate*, 35, 479–497.

Zheng, L. and Sun, J. (2016) The impact of vertical wind shear on the intensity and organizational mode of mesoscale convective systems using numerical experiments. *Chinese Journal of*

Atmospheric Sciences, 40, 324–340 (in Chinese). https://doi.org/10.3878/j.issn.1006-9895.1505.14311.

Zheng, L., Sun, J., Zhang, X. and Liu, C. (2013) Organizational modes of mesoscale convective systems over central East China. *Weather Forecasting*, 28, 1081–1098. https://doi.org/10.1175/WAF-D-12-00088.1.

Zheng, Y., Chen, J. and Zhu, P. (2007) Statistic characteristics and weather significance of infrared TBB during May–August in Beijing and its vicinity. *Chinese Science Bulletin*, 52, 3428–3435. https://doi.org/10.1007/s11434-007-0438-z.

Zheng, Y., Chen, J. and Zhu, P. (2008) Climatological distribution and diurnal variation of mesoscale convective systems over China and its vicinity during summer. *Chinese Science Bulletin*, 53, 1574–1586. https://doi.org/10.1007/s11434-008-0116-9.

How to cite this article: Guo, Y., Du, Y., Lu, R., Feng, X., Li, J., Zhang, Y., & Mai, Z. (2022). The characteristics of mesoscale convective systems generated over the Yunnan–Guizhou Plateau during the warm seasons. *International Journal of Climatology*, *42*(14), 7321–7341. https://doi.org/10.1002/joc.7647